A&A, 704, A274 (2025)
https://doi.org/10.1051/0004-6361/202555251

Astronomy & Astrophysics

Magnetic activity of M dwarf stars from the LAMOST DR10 medium-resolution survey

Wenjie Li[1], Liyun Zhang[1,⋆], Tianhao Su[1], Yinpeng Wang[1], Xianming L. Han[1,2], and Prabhakar Misra[3]

[1] College of Physics, Guizhou University, 550025 Guiyang, PR China
[2] Dept. of Physics and Astronomy and SARA, Butler University, Indianapolis, IN 46208, USA
[3] Department of Physics & Astronomy Howard University, Washington, DC 20059, USA

Received 22 April 2025 / Accepted 28 September 2025

ABSTRACT

Aims. M dwarf stars (red dwarfs) are the most common stars in the Milky Way (70% of all stars). Their temperatures and masses are low, but their magnetic activity is strong and includes flares, starspots, and coronal mass ejections. The internal structure and evolutionary processes of stars can be understood by studying their magnetic activity, as can their effect on the environments of surrounding planets. We used medium-resolution spectrum data of M dwarf stars from Data Release 10 (DR10) of the Large Sky Area Multi-Object Fiber Spectroscopic Telescope (LAMOST) to conduct a comprehensive and in-depth investigation of the stellar magnetic activity, flare, and starspot variations.

Methods. By cross-matching the low-resolution spectrum M dwarf star catalog from LAMOST DR10 medium-resolution spectrum data, we successfully identified 20 279 M dwarfs and obtained a total of 708 969 datasets of medium-resolution spectrum. These data provide a rich foundation for studying stellar magnetic fields and activity characteristics. Additionally, we cross-matched the data with light curves from the Transiting Exoplanet Survey Satellite (TESS), from which we acquired light-curve data for 2868 stars. We identified 891 flare stars in this sample, which provide an important sample for the statistical characteristics and physical mechanisms of flare events. By combining them with *Gaia* data, we clarified the characterisspatial distribution characteristics of M dwarfs in the Milky Way.

Results. Statistical studies of the magnetic activity of M dwarf stars based on LAMOST medium-resolution spectrum, showed that as the effective temperature of M dwarf stars increases, their stellar activity diminishes, although this trend becomes less evident for $T_{eff} > 3600$ K, and the amplitude of $H\alpha$ line variations increases strongly for later spectral types. In a sample of 11 868 M dwarfs with a signal-to-noise ratio higher than 10, we found that 1676 of the stars exhibited $H\alpha$ emission features, that is, were active stars. In the 891 flare stars identified from TESS light-curve data, we also detected 7496 flare events. Twenty-five of the 119 stars had $EW_{H\alpha}$ flare-like variations in TESS light-curve data. Research also clarified that the activity of M dwarf stars in the Milky Way decreases with increasing vertical distance from the Galactic disk. Furthermore, by combining LAMOST spectrum surveys with TESS light-curve data, a positive correlation between chromospheric activity as indicated by $H\alpha$ lines and the starspot area was established. Additionally, studies showed a positive correlation between the flare energy and their duration in M dwarf stars, and the slope of this correlation decreases for later spectral types. Finally, through analyzing the asymmetry of $H\alpha$ lines, two candidate coronal mass ejections were identified.

Key words. catalogs – surveys – stars: activity – stars: chromospheres

1. Introduction

M dwarf stars constitute 70% of the stellar population in the Milky Way and serve as a natural laboratory for studying the evolution of the Milky Way (Laughlin et al. 1997; Li et al. 2021). Their low brightness and small size make them ideal targets for the detection of exoplanet transits and radial velocity studies (García Soto et al. 2023). M dwarfs remain long on the main sequence and therefore provide favorable conditions for studying stellar magnetic activity and its effect on planets (Trifonov et al. 2018). They are also of significant value in the exploration of exoplanet civilizations and in tracing the chemical and dynamical history of the Milky Way (Li et al. 2021). For main-sequence stars, the stellar magnetic activity (e.g., flares, chromospheric activity, magnetic cycles, and starspots) is commonly observed in late-type stars, particularly in low-mass M dwarfs (Long et al. 2021). Solar flares are caused by magnetic reconnection in the stellar magnetic field and last from a few seconds to several days. They are a brief burst of energy that releases X-rays and ultraviolet, optical (especially in the blue visible part of the spectrum, e.g., the Ca II H&K and Balmer lines), infrared, and radio waves (Yang et al. 2017). Maehara et al. (2012) used high-precision photometric measurements from the Kepler Space Telescope K2 mission to discover many superflares, whose energies reach from 10 to 10^4 times the energy of the largest solar flares. Starspots and chromospheric heating of stars are both caused by magnetic activity on the stellar surface and correspond to changes in the stellar luminosity and in the emission of the $H\alpha$ line, respectively (García Soto et al. 2023). Their activity is driven by magnetic fields and manifests itself in phenomena such as flares, chromospheric heating, and starspots, which are closely related to the stellar age and rotation (Reiners et al. 2012; Long et al. 2021).

Stellar activity is commonly measured through emission in spectrum lines, particularly in the $H\alpha$ line, which reflects chromospheric activity and can indicate phenomena such as stellar winds, convective activity, or flares (Traven et al. 2015; Chang et al. 2017). Typically, the magnetic activity of stars is studied by

---

⋆ Corresponding author: `liy_zhang@hotmail.com`

quantifying the characteristics of their spectrum lines using the equivalent width (EW) of the $H\alpha$ line. The EW is an important parameter for measuring the intensity of emission or absorption lines. Typically, a negative EW indicates that the line is in absorption, suggesting a relatively quiet stellar chromosphere or weak magnetic activity. A positive EW indicates that the line is in emission, implying strong magnetic activity or active chromospheric processes in the star. Similarly, our investigation of magnetic activity in M dwarfs is based on the $H\alpha$ emission. Studies showed that stellar activity is correlated with the distance from the Galactic plane, and age gradients in the Milky Way were revealed (West et al. 2011). Advances in ground- and space-based telescopes have enabled large-scale studies of stellar evolution that provided insights into the relation between stellar activity, rotation, and convective envelopes (Zhang et al. 2016, 2021).

In the past two decades, the emergence of ground-based spectroscopic sky-survey telescopes and space photometric telescopes has led to a large amount of stellar optical data, which has provided an excellent resource for studying the statistical laws of stellar evolution. For example, West et al. (2008) used 38 000 stars from the Sloan Digital Sky Survey (SDSS) DR5 to verify the functional relation between stellar fraction and distance from the Galactic plane. West et al. (2011) used 70 841 M dwarfs from SDSS DR7 to study the relation between stellar magnetic activity and the Galactic plane. They confirmed that as the distance from the Galactic plane increases, the proportion of stars with magnetic activity gradually decreases. Zhang et al. (2016) analyzed data from 99 741 M stars in the Large Sky Area Multi-Object Fiber Spectroscopic Telescope (LAMOST) survey catalog and detected 6391 active dwarfs. Zhang et al. (2021) analyzed 738 477 low-resolution and 272 181 medium-resolution M stars from LAMOST to study stellar chromospheres and magnetic activity variations. They found that the variation rate in fully convective envelope stars (M 4 and later) is higher than that in stars with partially convective envelopes (M0–M3 dwarfs). Lu et al. (2019) studied the relation between chromospheric activity, flares, magnetic activity, and rotation periods using 480 912 M stars from LAMOST DR5. They found that the ratio of the flare frequency to the chromospheric activity index is consistent among M0-M3 dwarfs.

We analyze chromospheric activity and flare events in M dwarfs using LAMOST medium-resolution DR10 data. We used the desktop application TOPCAT for an interactive analysis of tabular data, particularly to analyze star catalogs (Taylor 2020). By cross-matching (search radius: 2 arcseconds) with *Gaia*, Transiting Exoplanet Survey Satellite (TESS), and VSX catalog, we obtained physical parameters such as the effective temperature ($T_{\rm eff}$, surface gravity ($\log g$)) and distance from the Galactic plane. This relatively small radius is suitable for the bright stars in our sample and effectively avoids contamination from unrelated sources. Similar methods have been adopted in other stellar surveys (e.g., Magaudda et al. 2022). While more sophisticated probabilistic cross-matching algorithms such as NWAY (Salvato et al. 2018) can provide quantitative assessments of matching reliability especially in crowded regions, we currently adopt the traditional nearest-neighbor method because it is practical and adequate for our target sample. We plan to explore these advanced approaches in future work. Section 1 highlights the importance of M dwarfs in studying exoplanets and Galactic evolution. Section 2 introduces the data we used, and Section 3 presents statistical analyses of chromospheric activity and flares. Section 4 focuses on the $H\alpha$ emission line variability and flare events, and Section 5 summarizes the key findings.

2. Data

2.1. LAMOST spectrum survey

The Large Area Multi-Object Fiber Spectroscopic Telescope also known as the Guo Shoujing Telescope, is a reflective Schmidt telescope with a large field of view and a large aperture. LAMOST operates in two observational modes: in medium (R≈7500) and low resolution (R≈1800). The effective optical aperture of LAMOST ranges from 3.6 to 4.9 meters, with 4000 optical fibers on the focal plane. A single exposure can capture spectra of 4000 celestial objects (Luo et al. 2012, 2015, 2022). The spectra of stars are initially processed through the LAMOST two-dimensional pipeline, followed by classification and radial velocity measurement using the one-dimensional pipeline (Luo et al. 2012, 2015). We classified the stellar spectra using LAMOST, specifically, the spectral type classification in LASPM, and we excluded M giant stars from the sample (Du et al. 2021). M giants and M dwarfs are very different. M giants are larger, their luminosity is higher and their temperature is lower, and their stellar lifetimes are different as well. It was therefore necessary to exclude M giants from the sample. We show the remaining sample is shown in the HR diagram in Figure 1. Our sample consisted of M dwarfs located on the main-sequence, without any M giants. We obtained their physical parameters, $T_{\rm eff}$, $\log g$, color index ($G_{\rm BP}$ - $G_{\rm RP}$), apparent magnitude (M_G) and metallicity through cross-matching with *Gaia* DR3 (Gaia Collaboration 2023). Our sample selection was primarily based on the spectral type (M dwarfs), and we did not apply any age-related filters (e.g., *Gaia* photometric color cuts). As a result, the sample may contain a small number of stars with varying ages, including some young pre-main-sequence stars, such as the scattered points with M_G>5 that lie off the main-sequence on the right side of Figure 1. There are only very few such young stars, and they account for only about 0.9% of the sample. They do not affect the main conclusions. By cross-matching the LAMOST DR10 low-resolution M dwarf star catalog with medium-resolution objects, we obtained 708 969 spectra of 20 279 M dwarf stars. The matched stellar spectrum data are listed in Table 1. The LAMOST name, RA, Dec, Lmjd, band, and S/N listed in the Table 1 were sourced from the LAMOST DR10 medium-resolution data[1]; $Low\_Subclass$ data originated from the LAMOST DR10 low-resolution data[2]; and *Gaia* MG, metallicity ([Fe/H]), and $BP-RP$ were obtained from *Gaia* DR3. $T_{\rm eff}$, Logg, and $[Fe/H]$ were obtained from cross-matching the TESS input catalog v8.2 using TOPCAT (Taylor 2020). We selected samples with a signal-to-noise ratio (S/N) greater than 10. We ultimately identified 11 868 M dwarfs that met this criterion. The spectral type distribution of these stars is shown in Figure 2. The left panel shows the distribution of the number of stellar spectra for various subtypes, and the right panel displays the distribution of the number of stars in each subtype. The figures clearly show that under the observational mode of LAMOST medium-resolution spectrum, the number of spectra obtained for each star is relatively high, and many stars have multiple exposures. To explore the nature of chromospheric activity in M dwarfs and its variations at different timescales, particularly on shorter timescales, multiple exposures of stars are beneficial to study these changes. We used the $H\alpha$ line as an indicator of chromospheric activity. First, we eliminated the cosmic-ray interference in the single-exposure spectra from LAMOST. To extract the continuum of

---

[1] `https://www.lamost.org/dr10/v1.0/medcas/search`

[2] `https://www.lamost.org/dr10/v1.0/catalogue`

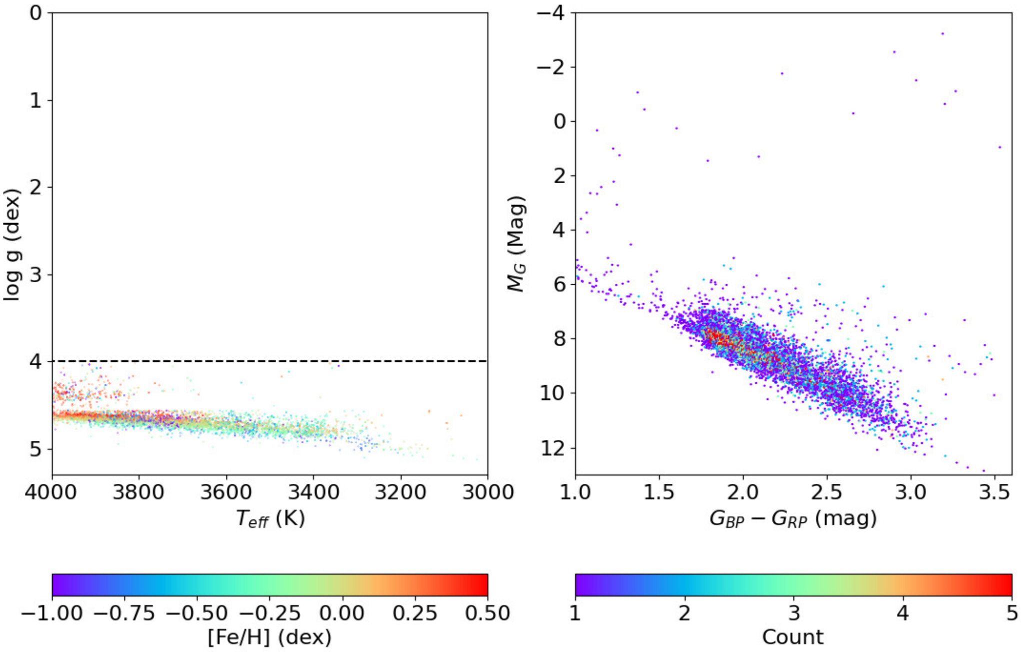

Fig. 1. Hertzsprung – Russel diagram of M dwarfs. The left panel shows the relation between the effective temperature ($T_{\rm eff}$) and the surface gravity ($\log g$). The metallicity ([Fe/H]) is colored. The right panel shows the relation between the color index ($G_{\rm BP} - G_{\rm RP}$) and the apparent magnitude (M_G). The number of stars is colored.

Table 1. Stellar parameters of M dwarf stars from LAMOST DR10.

LAMOST Name (1)	RA (2)	Dec (3)	med_lmjd (4)	med_band (5)	med_S/N r (6)	Low_Subclass (7)	T_{eff} (K) (8)	T_{eff}_err (9)	_Log g (10)	logg_err (11)	*GaiaMG*(*mag*) (12)	$BP - RP$(mag) (13)	$[Fe/H]$(dex) (14)
J034758.84+232904.2	56.99500	23.48414	58891	B	3.12	M5	3056.79	138.95	4.86	0.26	12.736	3.340	−0.380
J094033.11+382504.6	145.13822	38.41805	59183	R	5.3	M6	3200	106.71	5.27	0.27	12.572	3.272	−0.324
J005744.28+080550.6	14.43453	8.09715	59217	R	5.27	M5	3101.26	117.9	4.78	0.23	12.309	3.204	−0.228
J005744.28+080550.6	14.43452	8.09740	59217	R	5.27	M5	3241.6	129.91	5.2	0.31	12.309	3.204	−0.228
J141458.29+205314.4	213.74281	20.88714	58923	B	2.11	M5	3298.56	99.56	5.46	0.23	12.274	3.082	−0.382
J072111.49+333622.1	110.29807	33.60608	58883	B	4.31	M5	3297.12	96.08	5.3	0.21	12.151	3.027	−0.370
J090507.99+372528.9	136.28348	37.42468	59160	R	0.43	M4	3360.12	83.55	5.23	0.2	12.098	2.802	−0.416
J061034.44-091158.0	92.64354	−9.19949	59567	B	0.43	M5	3592.57	85.71	5.33	0.14	12.035	2.969	−0.374
J135758.21+262449.6	209.49253	26.41388	58943	R	0.51	M5	3177.34	96.12	5.1	0.2	11.932	3.037	−0.269
J041506.67+151951.8	63.77765	15.33117	58889	R	2.84	M5	3291.47	103.33	5.4	0.26	11.921	3.013	−0.244
J083925.40+295319.7	129.85561	29.88866	58863	R	20.31	M5	3335.21	80.85	5.36	0.19	11.859	2.948	−0.649
J035056.45+364834.3	57.73509	36.80970	59545	B	13.1	M5	3158.14	113.01	5.06	0.27	11.709	3.091	−0.011
J035056.45+364834.3	57.73517	36.80960	59545	B	13.1	M5	3243.82	105	5.14	0.26	11.709	3.091	−0.011
J120913.10+484841.6	182.30492	48.81165	58617	R	4.09	M3	3404.69	93.44	5.32	0.2	11.653	2.814	−0.742
J071157.56+172915.8	107.98998	17.48776	58888	R	0.4	M5	3271.14	100.49	5.22	0.25	11.623	3.006	−0.098
J111548.35+021852.9	168.95150	2.31472	59332	B	0	M4	3354.52	80.11	5.4	0.16	11.592	2.879	−0.236

Notes. Column (1): LAMOST name. Column (2–3): right Ascension, Declination. Column (4): local modified Julian day. Column (5): two values of *B* and *R*, which represent *B*- and *R*-band spectra. Column (6): signal-to-noise ratio. Column (7): spectral types in low-resolution search mode. Column (8): effective temperature from TESS. Column (9): effective temperature error. Column (10): surface gravity from TESS. Column (11): surface gravity error. Column (12): *Gaia G*-band magnitude. Column (13): $G_{\rm BP} - G_{\rm RP}$ magnitude. Column (14): metallicity. The full Table 1 is available at the CDS.

the red arm in medium-resolution spectrum, we applied a new spectral normalization method, using the spline function to process the spectra of M dwarfs. Then, we integrated the region around the $H\alpha$ line center, ±7.5 Å (illustrative examples of the continuum placement and Hα equivalent width measurements for stars with different activity levels are provided in the appendix (Figure A.1)) to calculate the EW of the $H\alpha$ line. This method was also used by Zhang et al. (2020a). We also cross-matched our sample with the 2-minute light-curve data from the TESS telescope and obtained light-curve data for 2868 stars. These were used to study stellar flares, starspots, and other activities.

2.2. TESS light-curve survey

The Transiting Exoplanet Survey Satellite space telescope was launched by NASA and was sent into orbit on April 18, 2018, on board the SpaceX Falcon 9 rocket. In the past five years, TESS has focused on conducting an all-sky survey to discover exoplanets orbiting nearby bright stars (Ricker et al. 2015). The TESS primary mirror consists of four identical cameras, each containing seven lenses, a set of detectors, and electronic components, with a lens sunshield. The combined field of view of the four cameras is 24° × 96°, and the survey can observe stars up to magnitude 13 (V <13) (Kossakowski et al. 2019). TESS possesses the observational capability to detect solid terrestrial planets and giant gas planets in potential orbits, effectively addressing the limitations of ground-based telescopes. Currently, TESS is observing 83 sectors located in orbit 174 and has successfully collected over 1.3 million light curves with 2-minute cadences. By conducting a detailed analysis of these light curves, we can more accurately trace dynamic changes in stellar surface activity, thereby uncovering potential connections between stellar magnetic activity and surface phenomena. Through cross-matching M dwarf samples with TESS observation sectors, we obtained light curves for 2868 M dwarfs, which provides a

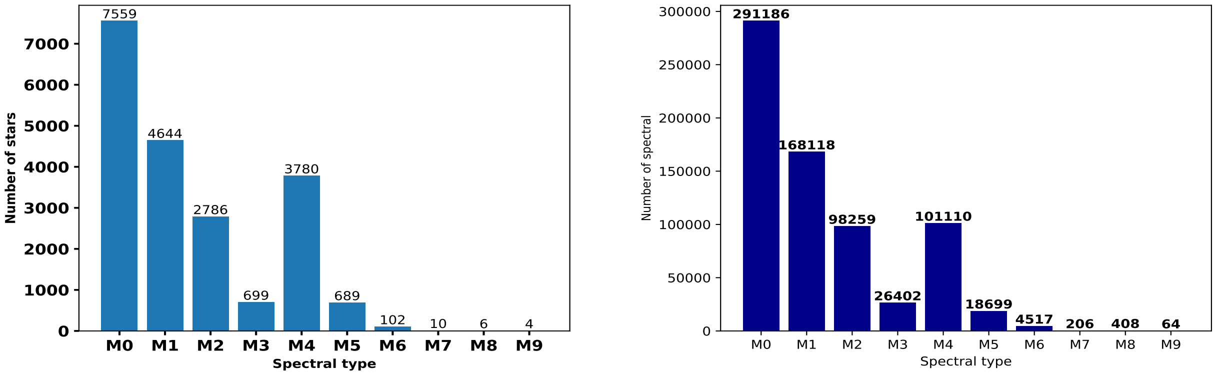

Fig. 2. Distribution statistics of the number of stars and spectra for each subclass. Left: bar chart showing the distribution of the number of stars in each subclass. Right: bar chart showing the distribution of the number of spectra for each subclass.

valuable dataset for studying the physical characteristics and activity behaviors of these stars. These light-curve data enabled us to conduct an in-depth investigation of the variability amplitude, periodicity, and potential starspot characteristics of M dwarfs. By analyzing the data, we can gain a more comprehensive understanding of the rotational periods, magnetic activity cycles, and the ways in which these properties evolve with stellar T_{eff} and mass.

3. Results and discussion of the stellar chromospheric activity

3.1. Stellar magnetic activity indicator: The Hα spectral line

Reiners & Basri (2008) established the magnetic activity threshold distinguishing inactive from active stars through an analysis of the $H\alpha$ emission line widths in late-type dwarfs. They systematically revealed a significant correlation between the activity levels and stellar rotation rates. Newton et al. (2017) extended these studies by systematically mapping the evolution of the magnetic activity with age in young stellar populations through measuring the $H\alpha$ line width. They revealed an activity saturation. Long et al. (2021) used the $EW_{H\alpha}$ to establish empirical relations between stellar activity levels (characterized by the EW) and fundamental parameters (e.g., mass and metallicity) through large-sample statistics. These studies not only established the methodological foundation of $H\alpha$ spectroscopic diagnostics for stellar magnetic activity, but more importantly, they revealed intrinsic connections between the activity strength and fundamental stellar parameters (e.g., rotation, age, and mass). Similarly, our investigation examines stellar magnetic activity through atomic line emission. By using $EW_{H\alpha}$ measurements, we systematically tested activity-parameter correlations. We applied the methods from Hawley et al. (2002) and West et al. (2004) to calculate the EW of the stellar spectrum as follows:

$$EW = \int_{Line} \frac{F_\lambda - F_c}{F_c} \mathrm{d}\lambda, \tag{1}$$

where F_λ is the line flux of the spectral line in the stellar spectrum, and F_c is the flux of the continuum at the two ends of the spectral line. West et al. (2004) calculated $EW_{H\alpha}$ using the trapezoidal integration method to sum the flux under the emission line. To determine the continuum flux F_c, they took the $H\alpha$ line center as a reference and selected spectrum ranges of 50 Å on either side: 6500–6550 Å for the left side, and 6575–6625 Å for the right side. This method is suitable for calculating continuum flux in low-resolution spectra, but for medium-resolution spectrum, its application in quantifying the $H\alpha$ line may have certain limitations. Therefore, we used a shorter continuum flux range at both ends of the line. Medium-resolution spectra provide finer detail than low-resolution spectra, and we therefore selected narrower spectral sections to avoid contamination from the continuum. This adjustment ensured the accuracy of the measurements, especially in the complex background around the $H\alpha$ line. The spectrum ranges we used (6500–6525 and 6610–6635 Å) are narrower than those in low-resolution spectra, which helped us to improve the quantitative accuracy of medium-resolution spectrum. Additionally, we adjusted the line width of the $H\alpha$ emission line to 15 Å (6555.85–6570.85 Å), which is slightly broader than the 14 Å used by West et al. (2004) and the 10 Å adopted by Han et al. (2023), which is an optimization based on the requirements of medium-resolution spectrum. This approach was taken to capture the shape of the emission line more accurately and to maximize the detection of subtle features in the wings of the $H\alpha$ line. Compared to low-resolution spectra, medium-resolution spectrum allow for a more detailed analysis of the line profile and thus provide a higher-precision when the $EW_{H\alpha}$ is measured. We list the $EW_{H\alpha}$ values for each star in Table 2. We plot the relation between T_{eff} and $EW_{H\alpha}$ for the sample in Figure 3. An $EW_{H\alpha}$ value of 0.75 was considered the baseline for $H\alpha$ line emission and was taken as the reference for M dwarf chromospheric emission. Figure 3 shows decreasing $EW_{\mathrm{H}\alpha}$ values of stars with rising effective temperature, although this declining trend becomes less pronounced at $T_{\mathrm{eff}} > 3600$ K. We performed a temperature-binned analysis by dividing the sample into several T_{eff} intervals and calculating the median $EW_{H\alpha}$ in each bin (red line). The results indicate that for stars with $T_{\mathrm{eff}} > 3600$ K, $EW_{H\alpha}$ remains relatively stable and shows no significant trend with increasing temperature. In contrast, for $T_{\mathrm{eff}} \leq 3600$ K, the $EW_{H\alpha}$ values exhibit a larger scatter and display a gradual decrease as T_{eff} increases. This trend indicates that the stellar activity gradually weakens with increasing temperature, which might be attributed to reduced chromospheric activity in higher-temperature M dwarfs. As T_{eff} increases, the $EW_{H\alpha}$ value gradually approaches or falls below 0.75, indicating that chromospheric activity is more significantly suppressed at higher temperatures. This aligns with our understanding of M dwarfs, where lower-temperature M dwarfs typically exhibit more active chromospheric activity. Figure 4 illustrates the differences in chromospheric activity among M dwarfs of various spectral types. The proportion of active stars increases with later

Table 2. Stellar parameters of M dwarf stars obtained through calculation and cross-matching.

LAMOST name (1)	$EW_{H\alpha}$ (Å) (2)	$EW_{H\alpha}$ err (3)	Mark (4)	Period (5)	Ro (6)	$R'_{H\alpha}$ (7)	τ (8)	Mass (9)	R(kpc) (10)	Z(kpc) (11)	Rad (12)	$EW_{H\alpha}$ bol (erg) (13)
J112911.62+022338.5	0.38136	0.0378	No	12.704	0.4096	8.44E-05	31.0191	0.506	8.3485	0.0881	0.508	1.90E+31
J102602.07+444349.3	−0.34724	0.0183	No			5.63E-05	21.9189	0.588	8.3993	0.0895	0.599	2.01E+31
J194512.12+454150.5	−0.41309	0.0165	No						8.3258	0.0144		2.19E+31
J094351.66-015602.4	3.25663	0.0437	Yes						8.3751	0.0487		2.20E+31
J140849.32+450543.9	−3.03648	1.5217	No						8.3392	0.0336		2.23E+31
J061534.35+213110.1	−1.04553	0.0462	No				39.9128	0.445	8.4222	0.0032	0.448	2.38E+31
J083053.60+190207.8	−0.44996	0.0393	No			9.80E-05	23.5737	0.571	8.4617	0.0785	0.58	2.49E+31
J035259.14+245405.5	1.93909	0.0638	Yes	2.494	0.1168	2.97E-04	21.361	0.594	8.4634	−0.0511	0.608	2.65E+31
J104134.79+041906.2	0.1666	0.0567	No				27.5805	0.534	8.3825	0.12	0.537	2.92E+31
J084446.47+124338.4	−0.07445	0.0909	No				19.5097	0.615	8.4718	0.0947	0.634	2.93E+31
J061017.76+223419.9	−0.20906	0.2584	No	0.69	0.0106	−4.12E-06	65.0366	0.323			0.341	2.95E+31
J035736.06+235552.3	1.9395	0.0404	Yes						8.4646	−0.0513		3.03E+31
J034408.80+230447.6	4.31042	0.1236	Yes						8.4604	−0.0568		3.06E+31
J064546.24+221524.2	−0.28836	0.0315	No						8.4884	0.0234		3.16E+31
J034607.51+242227.7	2.14014	0.0507	Yes						8.4593	−0.0532		3.62E+31
J150019.58+552238.0	−0.33509	0.0552	No			−1.36E-07	19.0913	0.62	8.3458	0.1734	0.8	3.67E+31

Notes. Column (1): LAMOST name. Column 2: $EW_{H\alpha}$ calculated from the dispersion spectrum. Column 3: $EW_{H\alpha}$ error. Column (4): Stellar activity classification: 'Yes' indicates an active star, and 'No' indicates an inactive star. Column (5): stellar rotation period. Column (6): Rossby number. Column (7): chromospheric activity index $R'_{H\alpha}$. Column (8): Stellar convective turnover time. Column (9): Stellar mass. Column (10): distance R from the point at which the spatial stellar position is projected onto the Galactic plane to the Galactic center. Column (11): distance perpendicular to the Galactic plane. Column (12): Stellar radius. Column (13): $EW_{H\alpha}$ energy value of flare-like variable stars. The full Table 2 is available at the CDS.

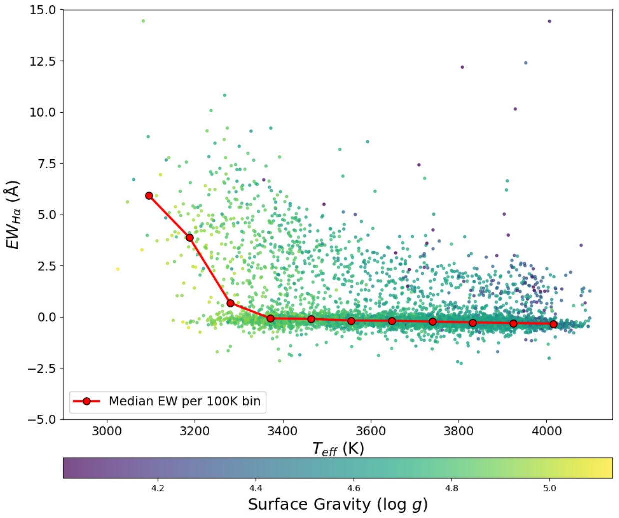

Fig. 3. Relation between T_{eff} and $EW_{H\alpha}$. The stellar surface gravity is colored. $T_{\rm eff}$ was obtained from cross-matching the TESS input catalog v8.2 using TOPCAT (Taylor 2020). The red line divides the stars into effective temperature intervals, indicating the median $EW_{H\alpha}$ within each interval.

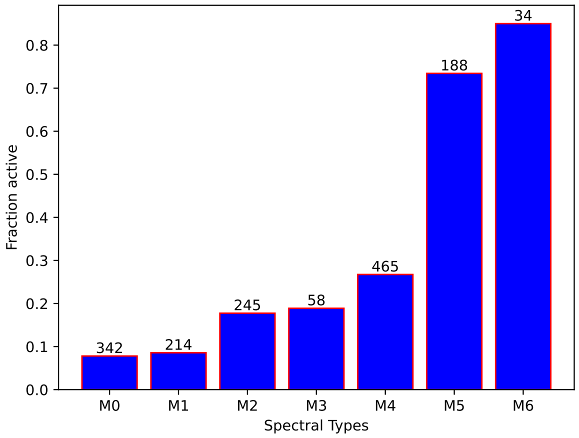

Fig. 4. Distribution of activity proportions for M dwarfs of different subtypes. The data labels represent the number of active stars.

spectral types, which further confirms that lower-temperature M dwarfs typically exhibit a higher chromospheric activity.

Magnetic activity occurs frequently in late-type stars, which makes it a significant aspect of study. Therefore, we focus on the chromospheric activity of M dwarfs. The molecular band structure is prominent in M dwarfs, and it is therefore challenging to directly obtain their true continuum. As a result, we adopted the standard proposed by Hawley et al. (2002) to assess the activity of M dwarfs. The criteria were as follows: 1. $EW_{H\alpha} > 0.75$. 2. The $EW_{H\alpha}$ value must be greater than three times the standard deviation, that is, $EW_{H\alpha} > 3\sigma$. 3. The emission strength of the $H\alpha$ line must be greater than three times the noise level at the line center. We identified 1676 M dwarfs in the 11 868 M dwarf stars with emission features, and the signal-to-noise ratio of these samples was greater than 10. The measurement data of our sample are listed in Table 2, which also includes parameters such as stellar rotation period, signal-to-noise ratio, spectral type, and stellar activity.

3.2. $H\alpha$ line variation

Stellar magnetic activity variations are often studied by analyzing changes in the $H\alpha$ spectral line. Kruse et al. (2010) investigated variations in the $EW_{H\alpha}$ values of the $H\alpha$ line to explore the evolution of stellar magnetic activity in multiple

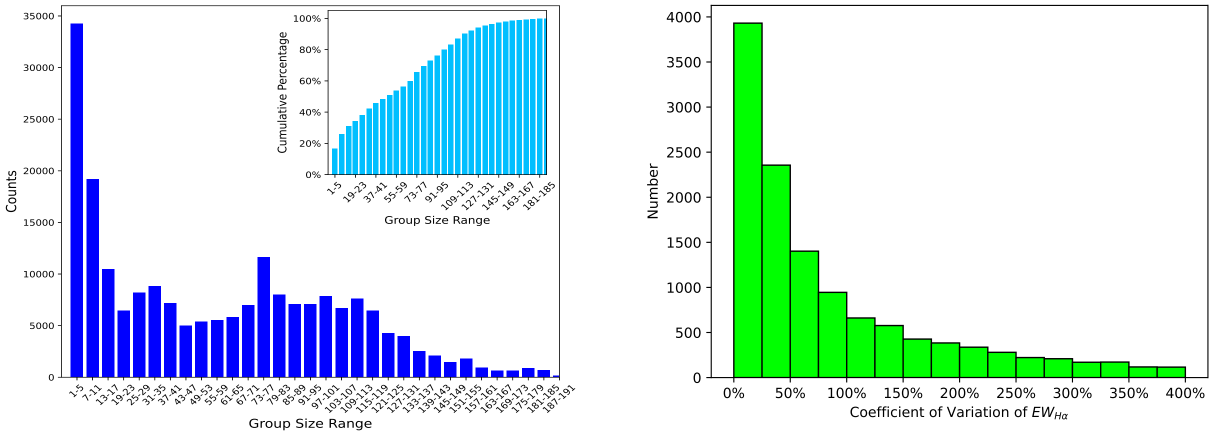

Fig. 5. Left: bar chart showing the distribution of the stellar exposure counts. The *x*-axis label refers to the binned ranges of exposure counts per star. Right: bar chart displaying the statistics of the variability coefficients for stars.

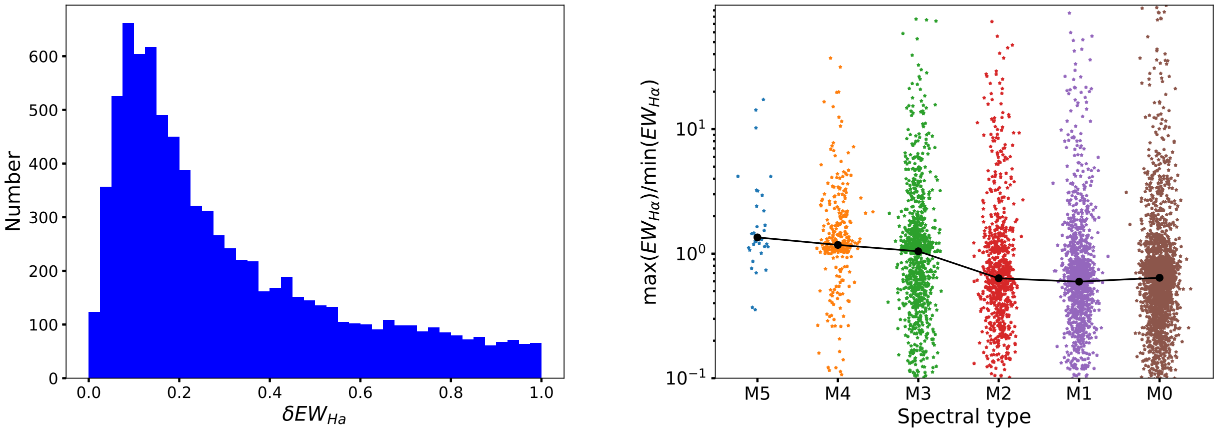

Fig. 6. Equivalent width (EW) of the $H\alpha$ line variation statistics. The left panel shows the distribution statistics of $\delta EW_{H\alpha}$ ($\delta EW_{H\alpha} = EW_{max} - EW_{min} > 3\sqrt{\sigma^2_{max} + \sigma^2_{min}}$) for each star. The right panel presents the distribution statistics of R_{EW} for each subspectral type, and the black line represents the median R_{EW} (R_{EW}=EW_{max}/EW_{min}) value for each subspectral type.

observations. Lee et al. (2010) and Kruse et al. (2010) used R_{EW} (R_{EW}=EW_{max}/EW_{min}) to quantify the variations in the $H\alpha$ line and concluded that the later the spectral type of the star, the greater the amplitude of the $H\alpha$ line variations. We calculated the coefficient of the variation (C.V.) for $EW_{H\alpha}$ (the C.V. is defined as the ratio of the standard deviation to the mean of the $EW_{H\alpha}$ values for each star. It simultaneously captures variations in dispersion and central tendency ($C.V. = \sigma/\mu \times 100\%$)) in the sample and statistically distributed the quantities of each C.V., as shown in Figure 5. The left panel shows the bar chart of the distribution of exposure counts for each star. The right panel illustrates the distribution of the $EW_{H\alpha}$ variation coefficients (C.V.) for the sample stars, where the number of stars decreases gradually as the coefficient increases. The variations in the $EW_{H\alpha}$ values for individual stars are plotted in Figure 6. The left panel presents the statistical distribution of $\delta EW_{H\alpha}$ ($\delta EW_{H\alpha}$ = EW_{max} - EW_{min} $>3\sqrt{\sigma^2_{max} + \sigma^2_{min}}$) for individual stars. The $\delta EW_{H\alpha}$ variation coefficients of most stars are concentrated between 0.1 and 0.2. Beyond a $\delta EW_{H\alpha}$ value of 0.1, the number of stars decreases as the variation coefficient increases. The right panel quantifies the variations in $EW_{H\alpha}$ using R_{EW}, and the black line represents the median R_{EW} for each spectral subtype. The figure shows that the variability in the $H\alpha$ line increases as the spectral type progresses to later types. This is consistent with the research findings of Bell et al. (2012) and Lee et al. (2010).

Gizis et al. (2002) used $EW_{H\alpha}$ to study the variations in stellar magnetic activity during repeated observations and found that as the standard deviation of $EW_{H\alpha}$ ($\sigma EW_{H\alpha}$) increased, the $EW_{H\alpha}$ value also increased. We calculated the $EW_{H\alpha}$ values in the sample, along with their corresponding standard deviations ($\sigma EW_{H\alpha}$) and the ratio ($\sigma EW_{H\alpha}/EW_{H\alpha}$), and we examined the relations between them, as shown in Figure 7. The relation between $EW_{H\alpha}$ and its standard deviation ($\sigma EW_{H\alpha}$), as well as the ratio of $EW_{H\alpha}$ to its standard deviation (σEW/$< EW >$), is shown in the figure. The red line reflects the trends and distribution characteristics of these variables, with results consistent with Gizis et al. (2002)'s study. We also present the spectral diagram of $H\alpha$ line variations and the $EW_{H\alpha}$ variation plot on short timescales, as shown in Figure 8. In the left panel, the spectral diagram clearly shows the variation in the $H\alpha$ line. In the right panel, the dynamic evolution of $EW_{H\alpha}$ on short timescales is presented. This variation plot clearly shows the fluctuations in the values of $EW_{H\alpha}$ over time, along with the corresponding changes in the associated features.

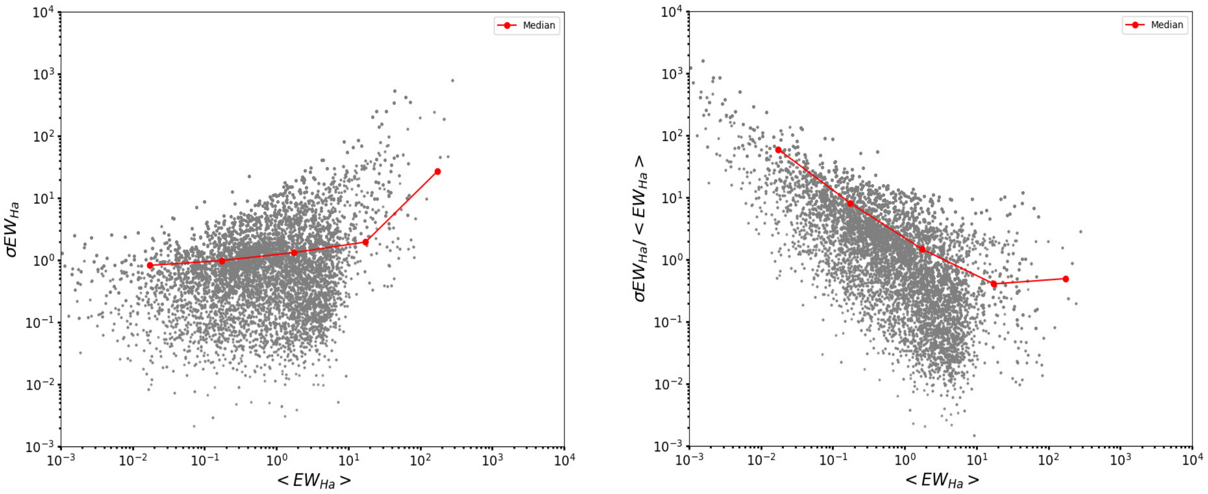

Fig. 7. Relation between $EW_{H\alpha}$, its standard deviation($\sigma\ EW_{H\alpha}$), and the ratio of the standard deviation to $EW_{H\alpha}$ is as follows ($\sigma EW_{H\alpha}/< EW_{H\alpha} >$): The left panel illustrates the relation between $EW_{H\alpha}$ and $\sigma\ EW_{H\alpha}$, and the right panel shows the relation between $EW_{H\alpha}$ and $\sigma EW_{H\alpha}/< EW_{H\alpha} >$. The red line represents the median value within each interval.

3.3. Stellar chromospheric activity index $R'_{H\alpha}$

The study of the stellar chromospheric activity is typically closely related to the stellar temperature and spectral characteristics. Figure 3 shows the significant correlation between the $EW_{H\alpha}$ and the effective temperature. In general, stars with lower temperatures tend to exhibit a stronger continuity in their magnetic activity. Under the condition of consistent activity levels, the $EW_{H\alpha}$ value is therefore expected to be higher. A more effective approach to analyzing stellar magnetic activity is to introduce a quantity that is independent of the stellar temperature and spectral type, however, namely $R'_{H\alpha}$. $R'_{H\alpha}$ is defined as the ratio of the line luminosity ($L_{H\alpha}$) in a stellar spectrum to its total bolometric luminosity (L_{bol}) (Walkowicz et al. 2004; Frasca et al. 2016). This ratio helps us to quantify the level of magnetic activity in the star, with higher values indicating stronger magnetic phenomena. Additionally, (Walkowicz et al. 2004) introduced the χ factor, which is independent of the stellar distance. The χ factor is a normalized parameter that describes the relation between a specific wavelength of the star (e.g., near the $H\alpha$ line) and its total radiation. It represents the ratio of the stellar surface continuous spectrum radiation flux near the $H\alpha$ line ($F_{H\alpha}$) to the total stellar radiation flux (the flux across all wavelengths, referred to as bolometric flux, or F_{bol}). This is expressed by the following formula:

$$\chi_{H\alpha} = \frac{F_{H\alpha}}{F_{bol}} = \frac{F_{H\alpha}}{\sigma T_{eff}^4}. \tag{2}$$

In the formula, σ represents the Stefan-Boltzmann constant, and T_{eff} is the effective temperature of the star. The χ factor normalizes the radiation flux near the $H\alpha$ line ($F_{H\alpha}$) by comparing it to the total stellar radiation flux (F_{bol}), effectively eliminating the influence of distance. This facilitates a comparison and study of the stars at different distances. The χ factor is particularly useful to study the stellar luminosity, temperature, and other characteristics, especially when a spectral analysis across different wavelengths is considered. When the stellar chromospheric activity indicator $R'_{H\alpha}$ is calculated, the distance-independent χ factor is therefore introduced to compute the ratio ($L'_{H\alpha}/L_{bol}$), as shown in the following formula (Walkowicz et al. 2004):

$$R'_{H\alpha} = \frac{L'_{H\alpha}}{L_{bol}} = \chi_{H\alpha}(EW_{H\alpha}). \tag{3}$$

The use of the $R'_{H\alpha}$ chromospheric activity indicator effectively eliminates variations in the continuous flux within specific regions of a stellar spectrum, which enables a better comparison of the stellar activity levels for dwarfs of different spectral types. This approach provides a reliable tool for studying the chromospheric activity features of various dwarf stars, reveals their behavioral differences under different environmental conditions, and offers essential data for the development of stellar evolution models. The calculated $R'_{H\alpha}$ values are listed in Table 2, and the distribution of $R'_{H\alpha}$ values for each star is shown in Figure 9. As shown, the log $R'_{H\alpha}$ values of the stars are generally in the range of −4.5 to −3.5. The distribution of $R'_{H\alpha}$ values and the distribution of active stars reported by West et al. (2004) and Newton et al. (2017) are broadly consistent with that of the active stars in our sample, which have $R'_{H\alpha}$ values around ≈3.5. West et al. (2004) reported that the log $R'_{H\alpha}$ values were mainly distributed in the range of −3 to −5, with active stars concentrated around log $R'_{H\alpha} \approx -4$. Newton et al. (2017) reported a distribution ranging from log $R'_{H\alpha} = -3$ to −6, where the active stars also cluster around log $R'_{H\alpha} \approx -4$. The double-Gaussian fit reveals two peak values at approximately −4.2 and −3.6 along the x-axis. This distribution may be influenced by factors such as the strength of the stellar magnetic activity and whether the stars exhibit flaring behavior.

3.4. The relation between chromospheric activity and stellar rotation

The factors that affect the strength of a stellar magnetic field include the depth of the convection zone, the effect of Coriolis forces, and the shear forces resulting from differential rotation. For hot stars, the heating mechanisms in the chromosphere and transition region are likely caused by acoustic-wave damping, whereas for cool stars, magnetic effects dominate. The transition in heating mechanisms between hot and cool stars occurs around the F5 spectral type (Simon & Drake 1989; Brito & Lopes 2019). Walter (1983) found that for stars near the F5 spectral type, the

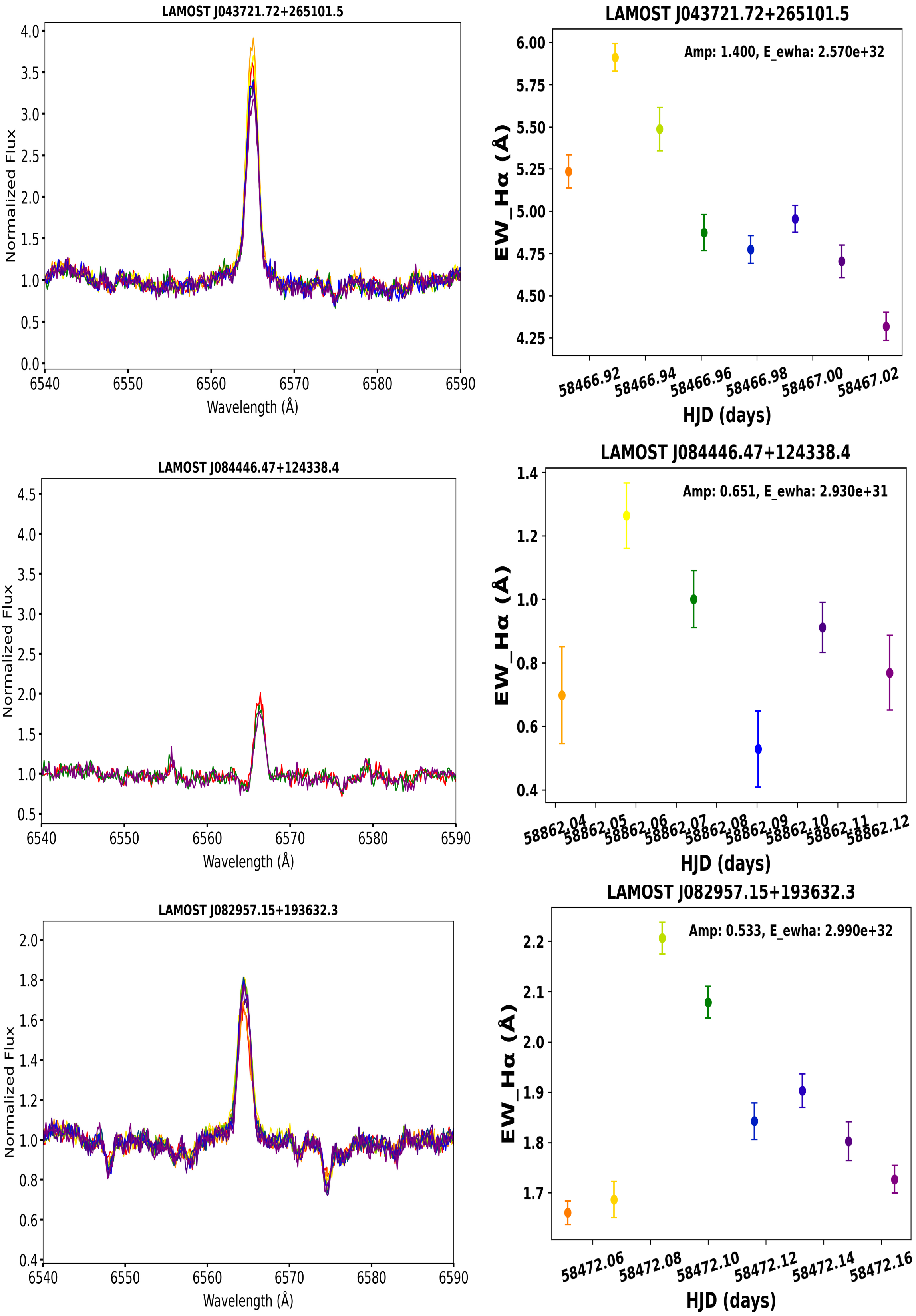

Fig. 8. $H\alpha$ variation in the selected examples. The left panel shows the spectrum that clearly displays the changes in the $H\alpha$ line. The right panel visually presents the dynamic evolution of $EW_{H\alpha}$ on short timescales, and the vertical red lines indicate the error bars. The colors of the spectral profiles in the left panel correspond to the points in the right panel, which are labeled with their respective heliocentric Julian dates, which allow a clear identification of the observation epochs.

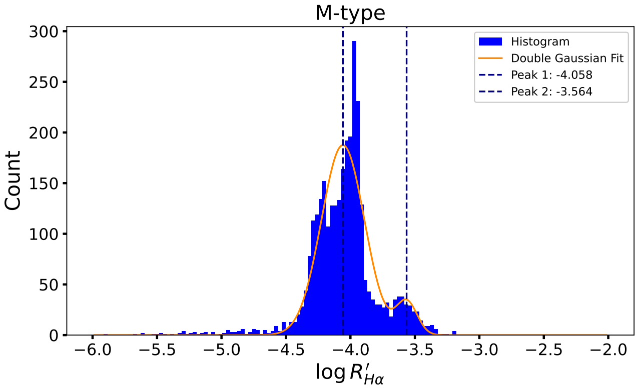

Fig. 9. Distribution histogram of a double-Gaussian fit of the $R'_{H\alpha}$ value. The x-axis represents the $R'_{H\alpha}$ values of each star, and the y-axis represents the number of stars.

relation between rotation and activity begins to emerge, which suggests that magnetic generation mechanisms similar to those of the Sun start to form.

Babcock (1961) used the α–Ω dynamo model to further investigate the relation between chromospheric activity, stellar rotation, and convection. This model is widely used to explain magnetic activity in late-type stars. Magnetic activity in late-type stars is typically triggered by differential rotation at different latitudes and by radial spiral effects (Mohanty & Basri 2003). This study also introduced the Rossby number (Ro) to analyze the relation between chromospheric activity and stellar rotation and convection (Noyes et al. 1984; Mamajek & Hillenbrand 2008). The Rossby number is defined as the ratio of the stellar rotational period (Prot) to the convective turnover time (τ), and it is expressed as Ro = Prot/τ. To more precisely investigate the relation between chromospheric activity intensity and the Rossby number, samples of binary stars from the VSX catalog and the TESS binary star catalog were excluded from the study (Watson et al. 2006; Green et al. 2023). By combining the TESS periodic star catalog and the VSX catalog, the rotation periods of the sample stars were determined, and the Lomb-Scargle (Lomb 1976; Scargle 1982; Fetherolf et al. 2023) method was applied to calculate the periods of 598 stars and identified whose periods were within the 10% error of the previous. Considering the limitations of TESS observations, we selected stellar samples with rotation periods ≥20 days and replaced them with the most reliable periods from McQuillan et al. (2013) and Sousa et al. (2019), among others. The TESS observations confirm a significant dependence on spectral type in the magnetic activity of early- to mid-M dwarfs. As demonstrated by Stelzer et al. (2022a) in their analysis of 112 M dwarfs, the reliable detection rate for the rotation period of M 4-M 5 type stars (≈11%), though lower than in the Kepler sample, shows that its flare rate peaks at M 3-M 4 spectral types. This finding, combined with the X1445 class superflare observed on AD Leo (M3.5) by Stelzer et al. (2022b), indicates that rapidly rotating early-M dwarfs remain significant sources of high-energy radiation. The calculation of τ was based on the empirical formula proposed by Wright et al. (2018), which correlates τ with stellar mass. The formula is as follows:

$$log\tau = 2.33 - 1.50(M/M_{\odot}) - 0.31(M/M_{\odot})^2. \quad (4)$$

In the formula, M represents the stellar mass. The stellar masses M was obtained from the TESS input catalog v8.2 (Stassun et al. 2019) by cross-matching using TOPCAT (Taylor 2020) with a matching radius of 2 arcseconds to identify the corresponding stars. The masses of late-type stars (M type and late-K type) were are further corrected based on the empirical M_{KS}-M_* relation established by Mann et al. (2019) from 62 nearby binary systems, which achieves an accuracy of 2–3% in the range of 0.075–0.70 $M_{\odot}$. The calculated values of Ro and the τ are listed in Table 2. Subsequently, the correlation between Ro and the chromospheric activity index $R'_{H\alpha}$ was analyzed, as shown in Figure 10. The horizontal axis represents Ro, and the vertical axis represents $R'_{H\alpha}$. The red and blue lines in the figure are the fit line of the sample, and this fit line was obtained according to the following formulas (Douglas et al. 2014; Newton et al. 2017):

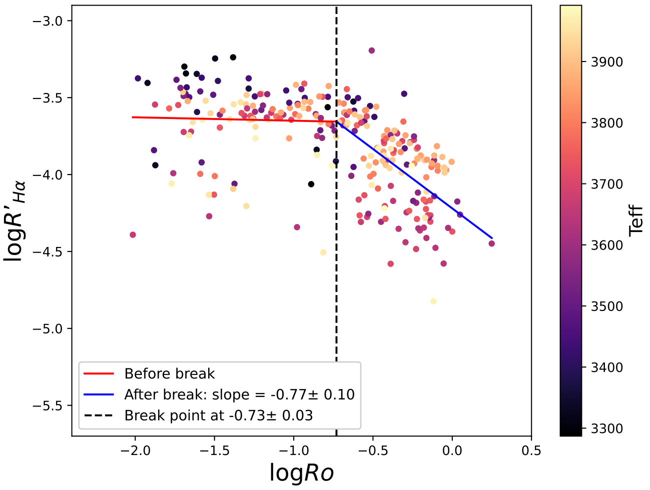

Fig. 10. Correlation between chromospheric activity indicators $R'_{H\alpha}$ and the Rossby number (Ro). The red and blue lines show the fit relation between these parameters. The color represents the stellar T_{eff}.

$$R'_{H\alpha} = \begin{cases} (R'_{H\alpha})_{sat} & Ro \le Ro_{sat} \\ CRo^{\beta} & Ro > Ro_{sat} \end{cases} . \quad (5)$$

In the fitting procedure shown in Figure 10, we employed a piecewise regression method. First, we restricted the candidate saturation point range to $[0.08, 0.4]$ to ensure that the slope of the fit tended toward zero in the leading segment and approached its most negative value in the trailing segment. This range was then discretized into 100 points, and linear fits were iteratively performed for each candidate saturation point, and we calculated the corresponding fit error. The point yielding the smallest error was chosen as the final saturation point. As shown Figure 10, the Ro_{sat} value displays a distinct decrease in slope at $Ro_{sat} = 0.18 \pm 0.03$. This phenomenon is associated with the critical point between saturated and unsaturated stellar activity. This critical point remains a topic of debate, however. For example, Douglas et al. (2014) reported a Ro_{sat} value of 0.11 ± 0.02, while Newton et al. (2017) found a value of 0.21 ± 0.02, Fang et al. (2018) determined the critical Ro_{sat} value to be 0.25, and Zhang et al. (2023) identified it as 0.12. The variation in the slope of the activity index and the threshold value of the Rossby number is attributed to differences in the sample selection, analytical methods, and the treatment of activity indicators in these studies. For our sample, the Ro_{sat} value was 0.18 ± 0.03, and the slope of the decrease in the unsaturated phase was −0.77 ± 0.01. The slope value is consistent with the error range reported by Douglas et al. (2014), which confirms that chromospheric activity in late-type stars systematically decreases with increasing Rossby number in the unsaturated regime.

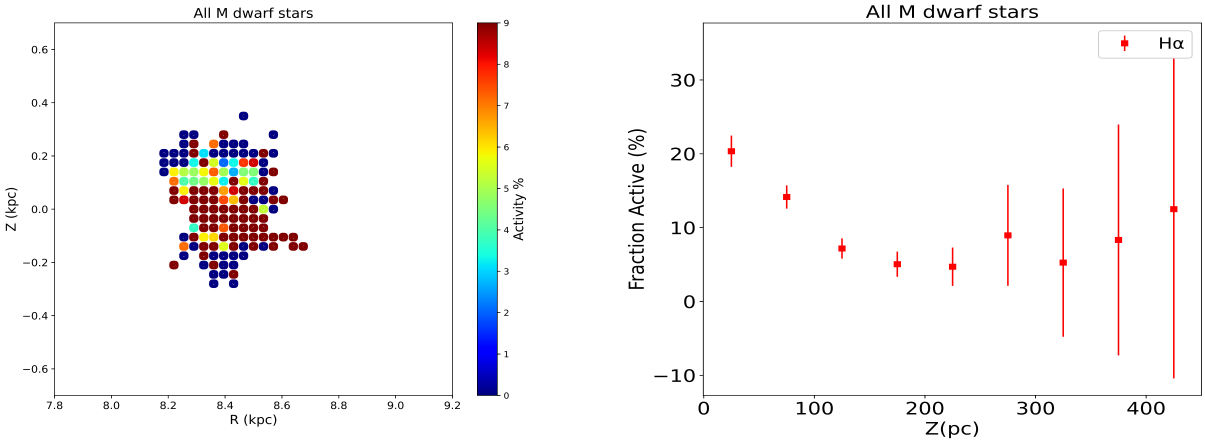

Fig. 11. Two-dimensional and one-dimensional distribution of active stars based on the *Hα* line. The left panel illustrates the two-dimensional distribution of the ratio of active stars to the total number of stars in cylindrical galactocentric coordinates (R and Z), where the color indicates the active fraction. The right panel shows the relation between stellar activity proportions and the vertical distance from the Milky Way plane. The vertical red lines represent the error bars.

3.5. Chromospheric activity distribution of M dwarfs in the Milky Way

Pineda et al. (2013) confirmed that the proportion of stellar activity decreases with increasing distance from the Galactic plane, and they explained this phenomenon as a consequence of the vertical age gradient of stars. We plot the distribution of the stellar activity proportions within the Milky Way for the sample in Figure 11. The left panel shows the spatial distribution of stellar activity proportions in the Milky Way, where R represents the distance from the projected point of the star on the Milky Way plane to the Milky Way center, and Z represents the vertical distance of the star from the Milky Way plane. The distribution of M dwarfs in the galaxy appears to be radial, with colors representing the activity proportions of the stars. The right panel shows the relation between stellar activity proportions and the vertical distance from the Milky Way plane. The results indicate that as the vertical distance from the Milky Way plane increases, the stellar activity proportion gradually decreases. This confirms the distribution of stellar activity in the Milky Way.

4. Stellar flares and starspots

Stellar flares are sudden intense energy releases on the surface of stars, where a large amount of energy is emitted in a short period. This causes a rapid increase in brightness. The shpae of the light curve is characterized by a fast rise and slow decay. Currently, astronomy is entering an era of long-term photometric monitoring, which provides a wealth of data and fosters the study of stellar flare characteristics (e.g., energy, frequency, amplitude, and duration). We used TESS light curves to search for flare events in the sample, systematically identified flare events in the TESS data, and calculated the flare energy and frequency for each event. Through a statistical analysis of these flare events, we plot the relation between flare energy and frequency, and compared the flare characteristics of different stellar types.

4.1. Search for stellar flares

Stellar flares are usually closely related to magnetic reconnection events. Magnetic reconnection is the process in which magnetic field lines reconnect and release a large amount of energy, either within a stellar interior or in its atmosphere. This process can lead to an intense energy release, resulting in flare phenomena. The intensity and frequency of flare events are typically related to the stellar magnetic activity and internal structure. Therefore, studying the mechanism of magnetic reconnection is crucial for understanding the origin of stellar flares. Hawley et al. (2014) conducted a detailed analysis of flare activity in M dwarfs using data from the Kepler survey, investigating the relations among flare frequency, energy distribution, and stellar magnetic activity in active and inactive M dwarfs. They found that mid-type M dwarfs (M3-M5) tend to exhibit frequent but low-energy flares. Davenport (2016) explored flare activity in M-type stars using TESS survey data and provided statistical characteristics of flare frequency and energy. They observed that complex multi-peaked events are more common in high-energy flares. Günther et al. (2020) studied M dwarf flares using TESS data and found that these flares can erode exoplanet atmospheres and impact habitability. Their results also confirmed that rapidly rotating M dwarfs have the most flares, and that flare amplitudes are independent of the stellar rotation period. In recent years, two main methods have been used to identify flares. One approach was to examine spectrum lines in raw spectra to spot flare events amidst strong background light curves, followed by detection in the detrended data. Another method involves using neural networks or machine-learning techniques to automatically identify and classify flare features (Feinstein et al. 2020). Both methods have their advantages, and they provide richer tools and approaches for the study of stellar flares. In most studies, the method of fitting background light curves to detect stellar flare events is commonly used (Gao et al. 2016; Lu et al. 2019; Günther et al. 2020). We also used the method of fitting background light curves to identify stellar flare events. By cross-matching our sample with TESS data, we obtained light-curve data for 2,868 stars and identified 891 flare stars. We extracted the SAP (PDCSAP) flux from the TESS light-curve data to search for flares. By optimizing the S/N, correcting the light-curve background, and removing systematics caused by satellite rotation using the common trend basis vectors, we calculated the average PDCSAP flux for each dataset, denoted as F_{ave}, using the following formula:

$$F_{ave} = \frac{F_{max} + F_{min}}{2}. \qquad (6)$$

Table 3. Stellar flare parameters of M dwarf stars.

LAMOST name (1)	Peaktime (2)	Begin (3)	End (4)	Duration (min) (5)	Amplitude (6)	E_{flare} (erg) (7)	R_{eff} (8)
J042039.18+271731.7	2510.849723	2510.74555	2510.952506	298.01664	0.095144	3.84E+35	0.082
J042751.42+185048.6	2523.325366	2523.212861	2523.397591	266.0112	0.103499	1.32E+35	0.015
J035259.14+245405.5	3249.482038	3249.436203	3249.618155	262.01088	0.180727	2.66E+35	
J044230.39+202710.8	3250.127425	3250.074644	3250.253821	258.01488	0.039633	5.31E+34	
J035733.93+244510.6	3257.732278	3257.696166	3257.873948	256.00608	0.035429	9.14E+34	0.004
J042736.58+192644.7	2508.592647	2508.585702	2508.755157	244.0152	0.449216	7.36E+34	0.016
J043304.51+263337.0	2516.898546	2516.849932	2517.009663	230.01264	0.108741	2.47E+35	
J043304.51+263337.0	2516.898546	2516.849932	2517.009663	230.01264	0.108741	2.47E+35	0.053
J041240.70+243815.4	3239.386897	3239.378563	3239.529961	218.01312	0.270266	2.36E+35	0.024
J043835.28+261036.8	2518.105496	2518.097162	2518.238836	204.01056	0.131942	3.29E+35	0.069
J175202.85+563628.7	2697.126371	2697.070814	2697.212483	204.00336	0.124293	1.42E+34	
J090227.85+584813.1	2606.570371	2606.560649	2606.702314	203.9976	0.281882		
J040704.28+332906.1	2913.500571	2913.456126	2913.596404	202.00032	0.451716	5.23E+35	
J041625.55+141016.7	2510.174846	2510.152623	2510.291519	200.01024	0.15508	2.10E+34	
J043214.57+182014.7	2524.135075	2524.130908	2524.269802	200.00736	0.085132		0.054

Notes. Column (1): LAMOST name. Column 2: flare peak time of stellar flare events. Column 3: flare onset time of stellar flare events. Column (4): flare decay time of stellar flare events. Column (5): Stellar flare duration. Column (6): Stellar flare amplitude. Column (7): flare energy of M dwarf stars. Column (8): Stellar starspot area. The full Table 3 is available at the CDS.

In this formula, F_{max} represents the maximum flux value, and F_{min} represents the minimum flux value. Next, the following formula was used to normalize the photometric data (PDCSAP flux):

$$F_{norm} = \frac{F_{PDC} - F_{ave}}{F_{ave}}. \tag{7}$$

In the above formula, F_{norm} represents the normalized result, where F_{PDC} is the PDCSAP flux. To improve the accuracy of the search results, we removed the variability of background stars from the normalized raw light curves. First, we excluded points in the normalized light curve that deviated by more than three times the standard deviation. Then, the remaining data were split and fit multiple times, and the best fit was selected as the background variability. The specific fitting process was described by Yang et al. (2023). In the dispersion sample of M dwarfs, we identified a total of 3653 flare events from 891 flare stars, and the parameters of these 3653 flare events are listed in Table 3.

4.2. Flare parameters

We calculated the flare energy of stellar flares using the following formula (Lu et al. 2019):

$$E_{flare} = 4\pi R^2 \sigma_{SB} (T)^4 \int F_{flare}(t) \mathrm{d}t. \tag{8}$$

In this formula, E_{flare} represents the flare energy of the star, F_{flare} is the normalized PDCSAP flux, σ_{SB} is the Stefan-Boltzmann constant, R is the stellar radius, and T is the effective temperature obtained from the TESS input catalog. The energy is expressed in erg. The calculated flare energy is listed in Table 3. Based on the calculated flare energies, the flare energy range of our sample is comparable to the results of studies by Tu et al. (2021), with an energy range of: $2.15 \times 10^{31} \backsim 1.07 \times 10^{36}$ erg. For the calculated flare energy results, as shown in Figure 12, the left panel shows the relation between the flare energy and the duration for all flare data samples, and the red line represents the fit result. The slope of the fit is 0.29, indicating a positive correlation. The right panel shows the relation between the log of the flare energy and the duration for all samples, and the color bar represents the number of flare events. The energy of most of the flare events lies in the range of 10^{32}–10^{34} erg.

Subsequently, the subspectral types within the M dwarf sample were distinguished to statistically analyze the relation between the flare energy and the duration across different spectral types. Figure 13 shows the relation between the flare energy and the duration for M dwarf stars of different subtypes. With increasingly later spectral type, the slope of the positive correlation in the fit results decreases gradually. The slopes of the fitting lines for the subspectral types of M dwarf stars were found to range between 0.29 and 0.43, indicating that the duration $t \propto E^{0.29-0.43}$. This result can be explained by magnetic reconnection theory, which suggests that the power-law index should be close to one-third. These studies confirmed this conclusion partially. For example, Namekata et al. (2017) used solar flare data and derived $t \propto E^{0.38\pm0.06}$. Tu et al. (2021) found that for solar-like stars in their sample, the relation between the flare energy and the duration was $t \propto E^{0.42\pm0.01}$. Figure 14 shows the relation between the log flare energy and the flare duration for M dwarf stars of different spectral subtypes. The longer the flare duration, the higher the flare energy. The color bar on the right represents the number of flare events. The figure also shows that for M dwarfs of different spectral subtypes, flare events with a duration shorter than 60 minutes are more common, while high-energy flare events tend to have longer durations. We also analyzed the relation between the stellar chromospheric activity and stellar starspots. To characterize the strength of stellar spot activity, we introduced the parameter R_{eff} (effective spot radius), which is a key derived quantity representing the characteristic scale of starspots. It is defined as the radius of a single circular spot that would produce the observed equivalent photometric modulation amplitude ($\Delta F/F$). The calculation of R_{eff} was adapted from the method proposed by He et al. (2015) and He et al. (2018). The core relation we used was

$$R_{eff} = 2(\sqrt{2} f_{rms}). \tag{9}$$

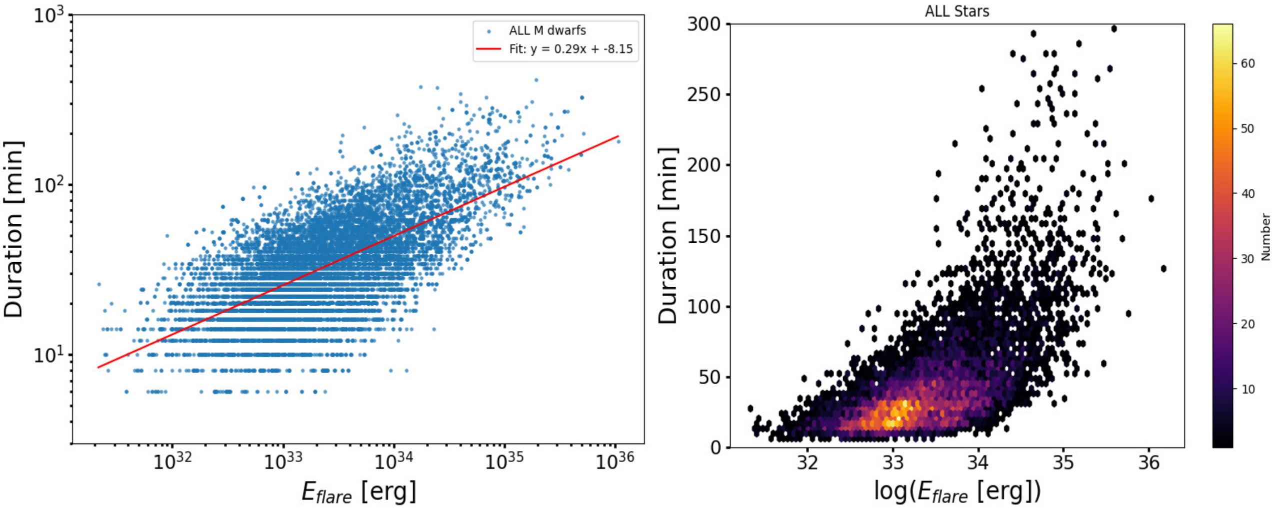

Fig. 12. Relation between stellar flare energy and duration. The left panel shows the relation between the flare energy and the duration for all flare data samples. The red line represents the fit result. The right panel shows the relation between Log(flare energy) and the duration for all samples. The color bar represents the number of flare events.

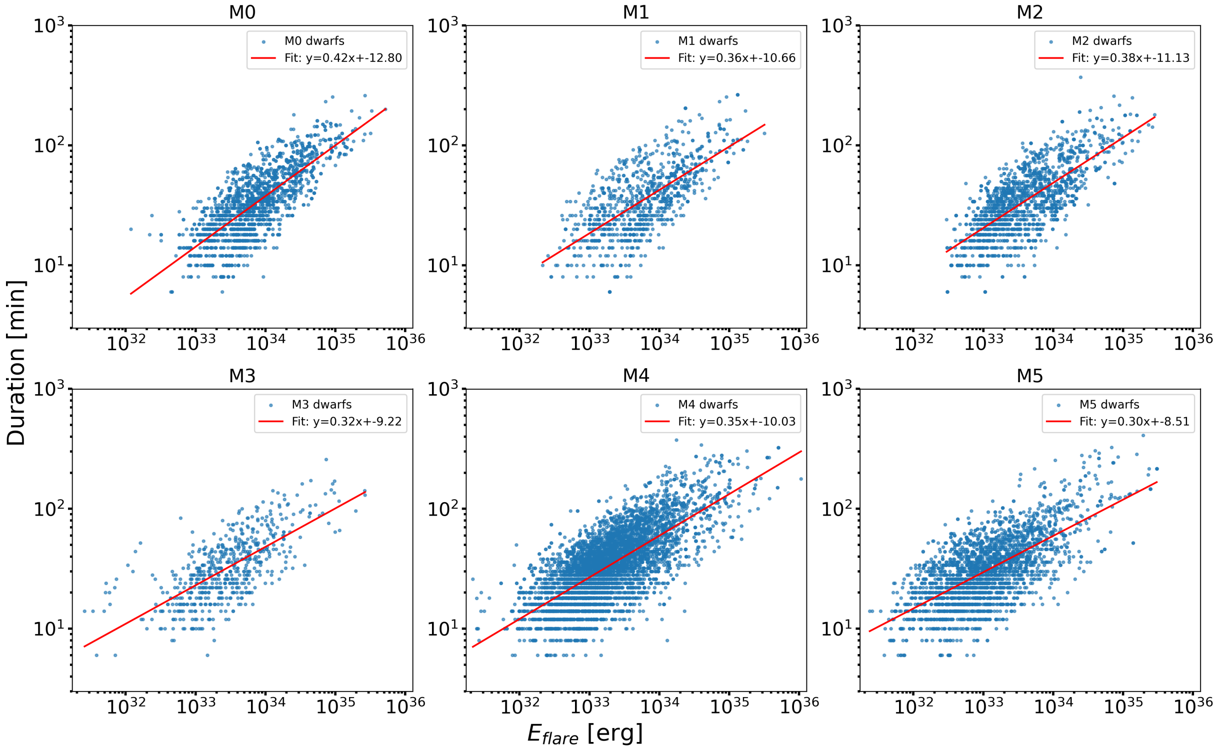

Fig. 13. Relation between flare energy and duration for M dwarf stars of different subtypes.

In the formula, f_{rms} represents the previously defined f_r (García et al. 2010; Chaplin et al. 2011), where f_r refers to the relative flux of each star after noise was remed. The coefficient preceding the formula serves as a correction factor, as proposed by He et al. (2015). Based on the TESS light curves and using methods established in previous studies (Zhang et al. 2020b), we calculated the amplitude of the photometric modulation caused by photospheric starspot activity. The left panel in Figure 15 shows the relation between the chromospheric activity indicator, $R'_{H\alpha}$, and stellar starspots, and the right panel shows the relation between $EW_{H\alpha}$ and stellar starspots. The fit lines show that the results are positively correlated, which indicates a positive correlation between the stellar chromospheric activity and stellar starspots.

We plot the distribution of the total number of flare durations and flare amplitude in Figure 16, where each subplot is a magnified version of the corresponding section in the main figure. The left panel of Figure 16 shows that the distribution of flare durations tends to decrease, and the highest number of events occur at a duration of 1.5 hours. The right panel shows that the distribution of the flare amplitude decreases as the amplitude increases, and the amplitude of most flare events lies in the range of 0.15.

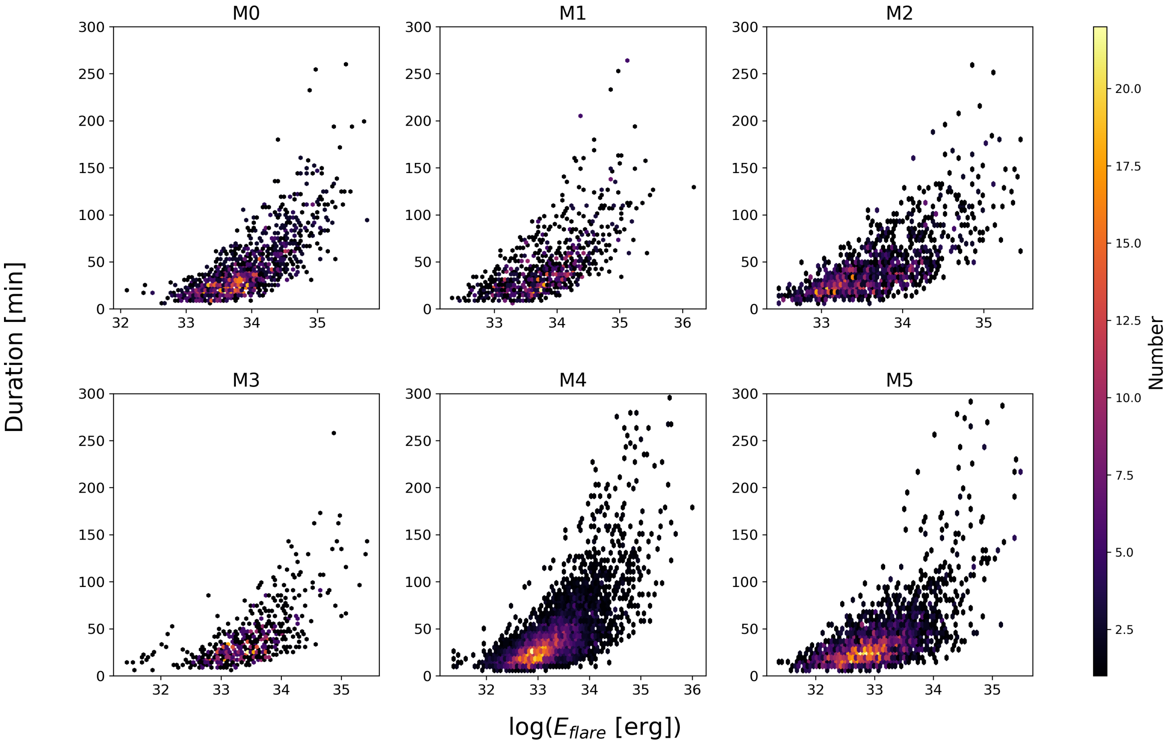

Fig. 14. Relation between the log flare energy and the flare duration for M dwarf stars of different spectral subtypes.

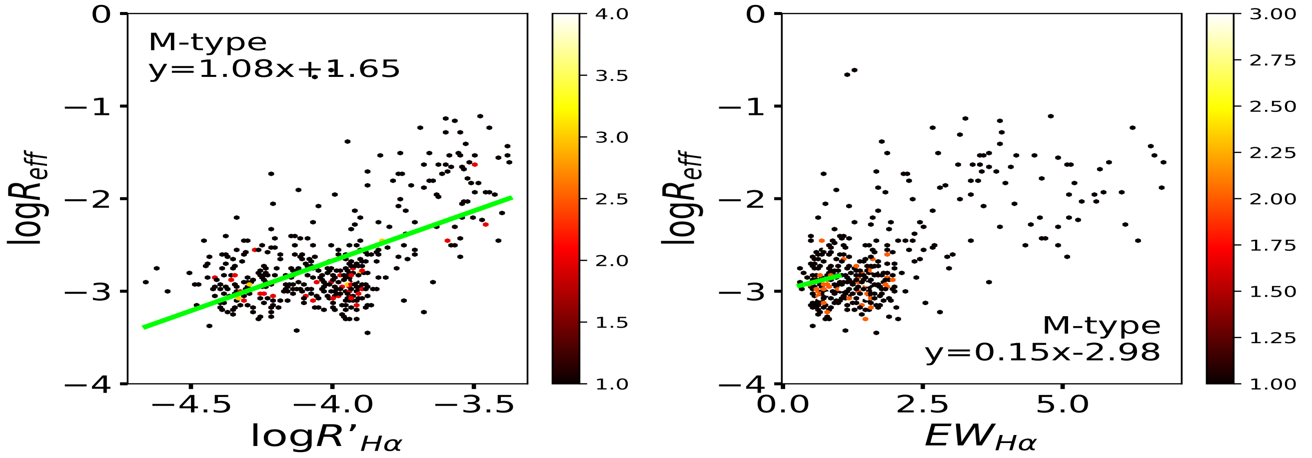

Fig. 15. Left panel: relation between the chromospheric activity indicator $R'_{H\alpha}$ and stellar starspots. Right panel: relation between $EW_{H\alpha}$ and stellar starspots.

We calculated the percentage of flare event durations and amplitude in different ranges relative to the total sample, as shown in Figure 17. The left panel shows the distribution of log flare durations, where the logarithm of the duration (log Dur) is primarily concentrated between −0.5 and 0.5, indicating that most flare events last between 10 minutes and 1 hour. The distribution is approximately normal, with a peak around $\log Dur \approx -0.2$, meaning that these flare events lasted around 40 minutes. The right panel shows the distribution of log flare amplitude, with log Amp concentrated between −2 and −1, indicating that most flare events have relatively small amplitude increases. The peak occurs around $\log Amp \approx -1.6$, suggesting that the amplitude of most flare events lies in the range of 0.025. Overall, these two charts show the percentage distribution of flare event duration and amplitude in different ranges, revealing that their distributions are close to normal, with distinct peak regions for each. Next, in our study of the $H\alpha$ line variations, we specifically searched for flare-like changes in the $H\alpha$ line, including rapid rises and slow decays in the $EW_{H\alpha}$ values. We identified 119 stars with $EW_{H\alpha}$ flare-like events and calculated the energy and amplitude of the $EW_{H\alpha}$ variations for these events (Wu et al. 2022). The energy ranged from 6.12×10^{28} to 3.05×10^{35} erg. The specific steps for calculating the $EW_{H\alpha}$ energy were based on Wu et al. (2022), and the results are listed in Table 2. Several clear representative examples were selected to illustrate typical $EW_{H\alpha}$ flare-like events observed in our sample. The $EW_{H\alpha}$ variation diagrams of these events are presented in Figure 18, showing changes in $H\alpha$ on short timescales. This figure shows the changes in the $EW_{H\alpha}$ energy and amplitude on this timescale, and it reveals a trend of a rapid rise and slow decay in the

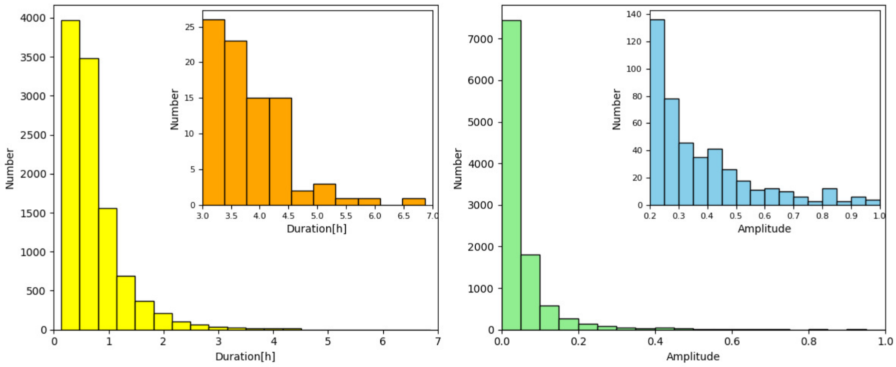

Fig. 16. Number distribution of the stellar flare duration and flare amplitude. The left panel shows the number distribution of stellar flare durations, and the right panel shows the number distribution of the flare amplitude.

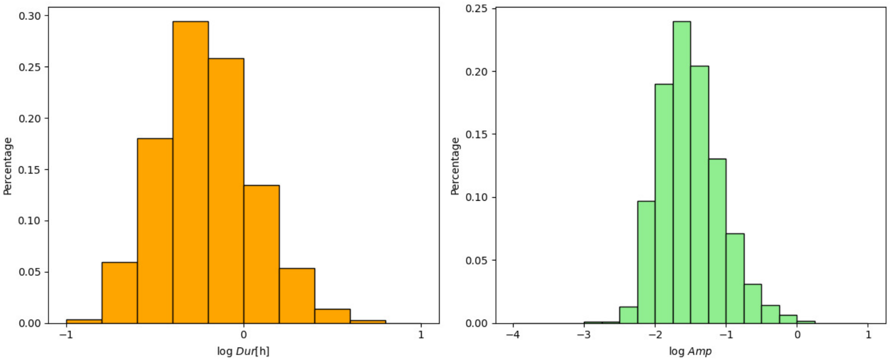

Fig. 17. Percentage distribution of the flare event duration and amplitude in different ranges relative to the total sample. The left panel shows the distribution of the flare duration percentages, and the right panel shows the distribution of the flare amplitude percentages.

$EW_{H\alpha}$ values. Twenty-five of the 119 stars with $EW_{H\alpha}$ flare-like variations were flare stars.

4.3. $H\alpha$ asymmetry

A stellar flare is a violent release of energy from the stellar surface that typically converts magnetic energy in the corona into kinetic and thermal energy through magnetic reconnection. It is often accompanied by CMEs. Stellar flares and CMEs can affect the magnetic field and ionosphere of a planet and might erode or strip away the planetary atmosphere, thereby affecting the habitability of the planet (Shibata & Magara 2011; Temmer 2021; Cliver et al. 2022). Observations of stellar optical spectra can provide important indications of stellar CMEs. Currently, the detection of stellar CMEs mainly relies on the Doppler-shift method, which identifies them through the emission or absorption enhancements in spectrum lines. Namekata et al. (2022) investigated the superflare on the young Sun-like star EK Dra through detecting the $H\alpha$ spectrum. The blueshifted absorption observed in the $H\alpha$ spectrum is considered evidence of a massive stellar filament eruption. Lu et al. (2022) identified three stellar CME candidates by examining the asymmetry of the $H\alpha$ spectral profiles. Wang et al. (2024) and Xu et al. (2025) also confirmed two objects with an $H\alpha$ asymmetry by analyzing the symmetry of their $H\alpha$ spectral profiles. We used the Doppler-shift method to search for potential stellar CMEs in the LAMOST sample of dispersed M dwarf stars. In the search for stellar CMEs, we identified them by inspecting the asymmetry of the $H\alpha$ spectrum lines in LAMOST medium-resolution spectra. There are various methods to determine the asymmetry of spectral profiles (Maehara et al. 2021; Koller et al. 2021). We quantified the asymmetry of the $H\alpha$ spectral line by calculating the difference in the integrated areas on either side of the $H\alpha$ profile peak. We normalized the LAMOST medium-resolution spectrum using the average flux of the spectrum as the reference, as shown by the baseline (horizontal black line) in Figure 19. The dashed red and green lines represent the integration boundaries, and the dashed yellow and blue lines indicate the theoretical and actual peak values of the $H\alpha$ profile. To determine whether the $H\alpha$ spectral line shows a redshift or a blueshift, we plot medium-resolution $H\alpha$ spectrum for individual spectra. By calculating the peak flux ratio (0.2, 0.4, 0.6, and 0.8), which represents the fraction of the spectral flux above the baseline, after subtracting it from the peak, we analyzed the differences in the line profile distribution between the two sides. when the average difference between the two sides exceeded 0.56 Å (with an error of 0.14 Å per region), a redshift or blueshift was identified. We simultaneously examined all spectra and cross-matched them with the SIMBAD database (Wenger et al. 2000), excluding pulsating variables such as eclipsing binaries, T Tauri stars, and RR Lyrae stars, which might affect the $H\alpha$ spectrum lines. We identified 289 medium-resolution $H\alpha$ spectra with blueshifts or redshifts, from which we identified two objects with $H\alpha$ asymmetry features.

4.4. Stellar CME candidates

To identify CME candidates, we searched for potential CME candidates by detecting red- or blueshifted asymmetries in spectral stellar $H\alpha$ lines. In 289 objects with red- or blueshifted spectrum lines, the $H\alpha$ asymmetry sample was identified through visual inspection. Using the methods described above and through manual inspection of the identified candidates, we ultimately confirmed two stars as CME candidates. CME candidate 1 is an M2-type main-sequence star (LAMOST J133213.26+505702.2),

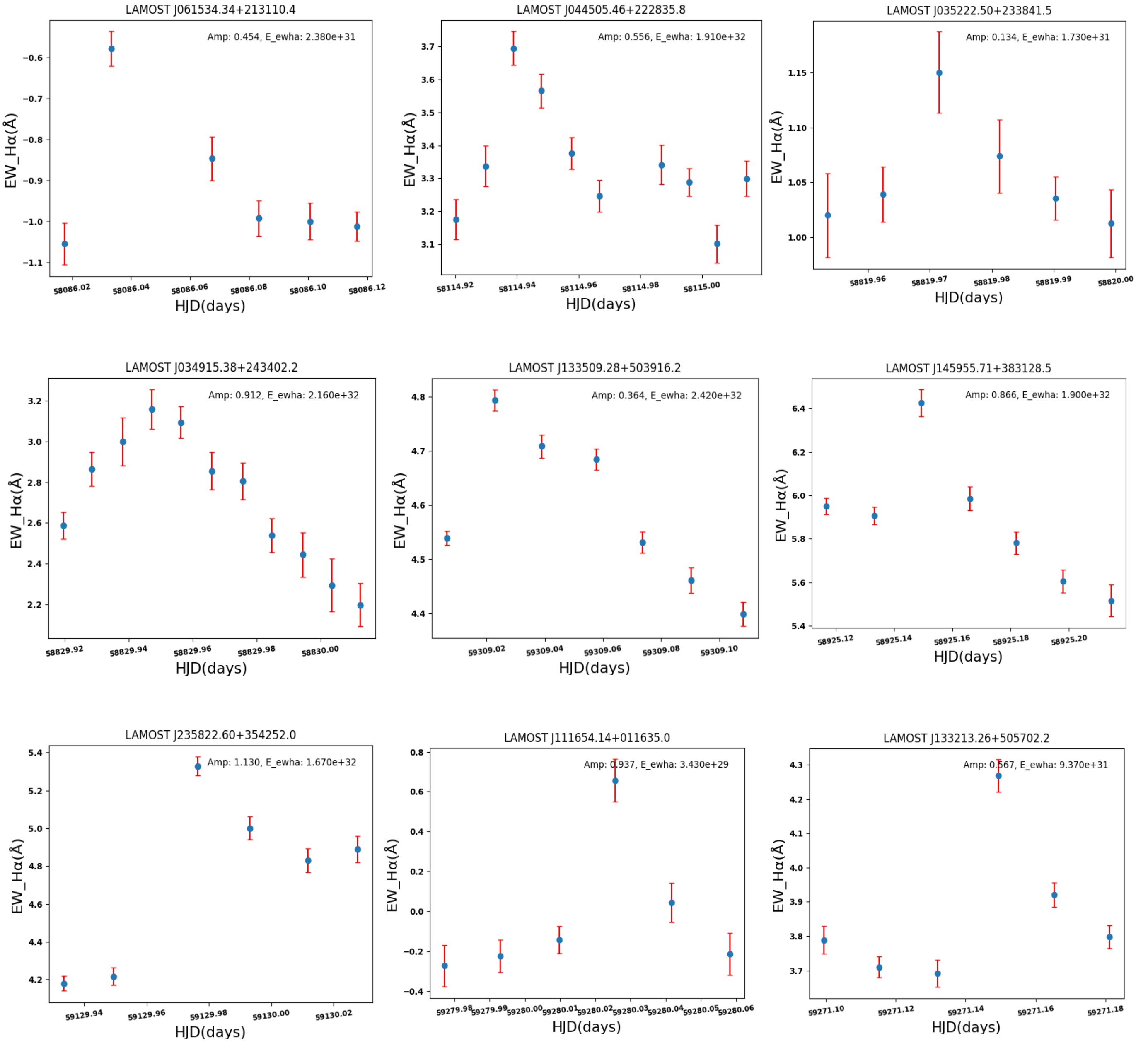

Fig. 18. Dynamic evolution of the $EW_{H\alpha}$ on short timescales. The values of the $EW_{H\alpha}$ energy and amplitude changes are shown, and the vertical red lines indicate the error bars.

which is also the flare star TIC 320351354. The LAMOST medium-resolution spectrum of this star consists of three consecutively observed subspectra. Figure 20 displays the stellar spectra, with the left panel showing the three preprocessed $H\alpha$ spectra, and the middle panel showing the smoothed $H\alpha$ spectra. The first two spectra (blue and orange lines) are slightly asymmetrical, with minor variations in the intensity of the $H\alpha$ emission. They are largely consistent with each other, however, which indicates that the $H\alpha$ emission in these two spectra remains relatively stationary with respect to the stellar system. We therefore used the first spectra as reference spectra. The third spectrum (green line) shows a clear enhancement of the red wing and asymmetry, representing the active spectrum. We compared the active spectrum with the reference spectrum using a double-Gaussian fit, and the fit results are shown in the right panel. This method refers to the work of Lu et al. (2022), with the vacuum wavelength data of the $H\alpha$ spectral line obtained from van Hoof (2018). From the fit contrast profiles, the dashed blue and red lines exhibit redshift components. This phenomenon is likely caused by chromospheric condensation or coronal rain (Canfield et al. 1990; Lu et al. 2022; Cao et al. 2023). Coronal rain is the phenomenon in which condensed plasma in the corona of the Sun or a star falls back from higher atmospheric layers to lower ones (e.g., the chromosphere) along magnetic field lines under the influence of gravity. Because this process looks like falling rain, it is called “coronal rain”. We calculated the radial velocity of the third spectrum to be 76.38 km/s. This velocity falls within the typical range of coronal rain velocities (30–150 km/s) (Oliver et al. 2016; Lu et al. 2022), and we therefore conclude that coronal rain is the primary cause of this phenomenon. After cross-analyzing TESS data, we obtained the light curve of the star. Stellar flares were clearly identified

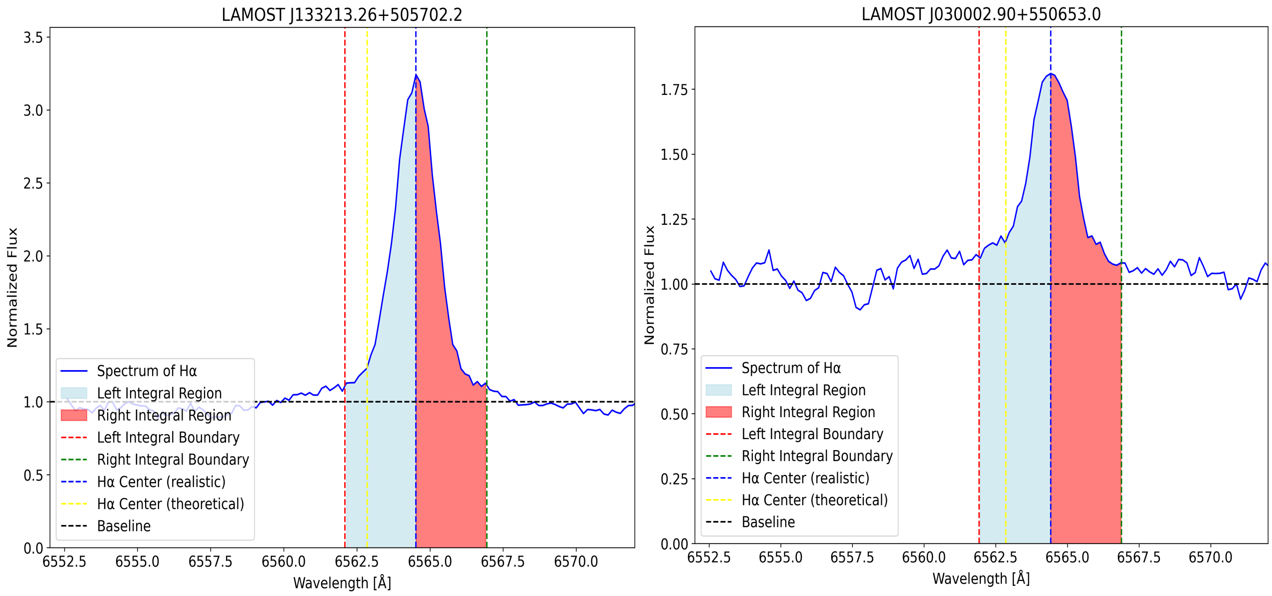

Fig. 19. Examples of the $H\alpha$ profile asymmetry in stellar redshift and blueshift integration regions for CME detection. Left: LAMOST J133213.26+505702.2. Right: LAMOST J030002.90+550653.0. The dashed red and green lines represent the integration boundaries, the dashed yellow and blue lines indicate the theoretical and actual peak positions of the $H\alpha$ profile, and the light blue and red regions represent the integration areas.

in the light-curve data. The cooling phase following these flare events might be one of the factors that contribute to the redshift observed in the $H\alpha$ spectral line. During the cooling phase following a flare, some plasma becomes thermally unstable, condenses, and falls toward the lower atmosphere along magnetic field lines, forming coronal rain. The lower panel of Figure 20 illustrates the identified flare events in the stellar light curve, along with a magnified view of the corresponding flare regions.

The CME candidate 2 (LAMOST J030002.90+550653.0) was identified as a high proper motion star through cross-matching with the SIMBAD database. A flare event for this star was also detected in the TESS light-curve data (TIC 251469806). The LAMOST medium-resolution spectrum of this star consists of four consecutively observed subspectra. Figure 21 shows the spectrum of this star. The first and second of these $H\alpha$ spectra (blue and orange lines) have similar shapes and emission strengths for the $H\alpha$ line, and thereby, we considered them as reference spectra. In contrast, the third and fourth spectra (green and red lines) clearly show an increase in the $H\alpha$ line emission strength, asymmetry in the line, and a blueshift. Therefore, we considered these two spectra as active spectra. After we performed a double-Gaussian fit on the contrast spectrum profile (see the right panel of Figure 21), the fitting results revealed a blueshifted (red line) component and a broad emission component (blue line) centered around other wavelengths of the $H\alpha$ line. The radial velocity of its active spectrum is 71.61 km/s. The blueshifted component in the $H\alpha$ line profile might originate from CME eruptions along the line of sight, while the broad emission component (blue line) in the double-Gaussian fit might be related to Stark broadening caused by electron acceleration (Muheki et al. 2020; Wu et al. 2022). By cross-matching with TESS data, we obtained the stellar light curve, which revealed flare events through analysis. We suggest that the blueshift observed in the $H\alpha$ spectral line might be associated with a CME that accompanied the stellar flares.

Although we identified two CME candidate events based on asymmetries in the $H\alpha$ line, spectral features alone are not sufficient to confirm the existence of CMEs. To further verify these candidates, we searched the 3XMM-DR5 catalog (He et al. 2019) and the study by Wang et al. (2020) on X-ray activity, but found no corresponding X-ray observations for the two stars. The lack of simultaneous X-ray and TESS observations prevents us from providing additional supporting evidence. At present, multiwavelength coordinated observations of M dwarfs remain challenging. In the future, combined monitoring with optical, X-ray, and space-based photometric data may help us to improve the reliability of a CME identification.

5. Summary

We used the TESS light-curve data of 2868 M dwarfs and 20 279 stars from the LAMOST MRS DR10 to investigate stellar chromospheric activity and flare events. The chromospheric activity was determined based on the $EW_{H\alpha}$ and the $R'_{H\alpha}$ index to assess the stellar chromospheric activity. The $EW_{H\alpha}$ values were calculated for 16 504 M dwarfs, 11 868 of which had a signal-to-noise ratio greater than 10, and 1676 of these M dwarfs were identified as active stars. The distribution of the stellar activity by spectral subtype showed that the activity ratio increased with later spectral types. A sudden rise in activity was observed between M4 and M5, which was attributed to the fact that stars of spectral types M4 and later are fully convective, whereas earlier types are not. By using the chromospheric activity indicator, $R'_{H\alpha}$, and combining it with Ro, we minimized the effects of continuous flux variations specific to the stellar spectral regions, which allowed us to study the stellar magnetic activity more accurately. Based on the correlation between Ro and $R'_{H\alpha}$, we conclude that at $Ro_{sat} = 0.18 \pm 0.03$, the stars in this sample reach the critical point between saturated and unsaturated phases. The slope of the decline in the unsaturated phase is -0.56 ± 0.07. By combining the *Gaia* data, we clarified the spatial distribution of M dwarfs in the Milky Way and studied the distribution of stellar magnetic activity. M dwarfs display a radial distribution in the galaxy, with a higher proportion of active stars in regions closer

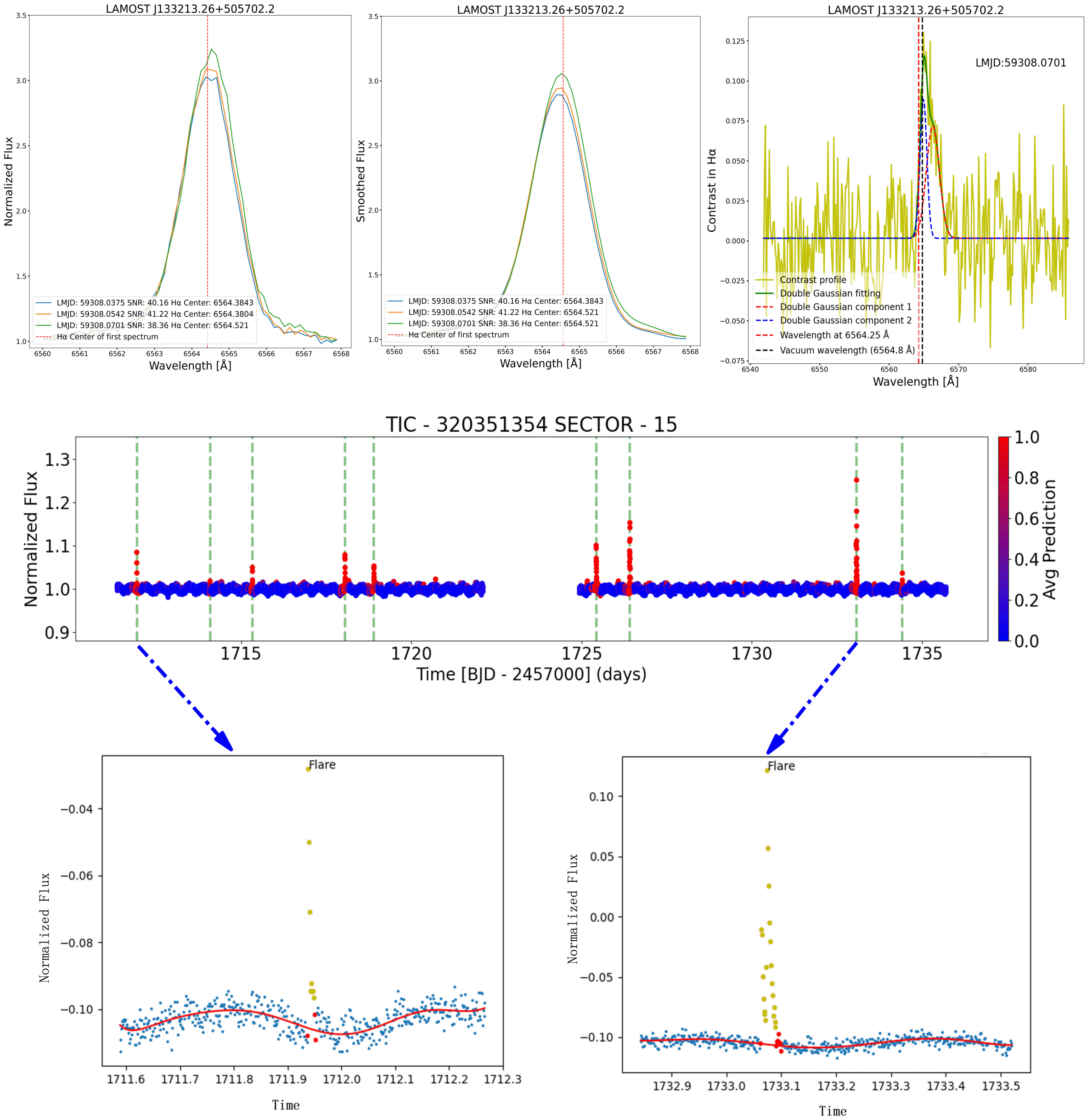

Fig. 20. Spectral analysis of the stellar $H\alpha$ lines and double-Gaussian fit. The left panel shows the preprocessed $H\alpha$ spectra of the star, the middle panel presents the smoothed $H\alpha$ spectra, and the right panel displays the contrast flux profile derived from the double-Gaussian fit. The lower panel illustrates the identified flare events in the stellar light curve along with a magnified view of the corresponding flare regions.

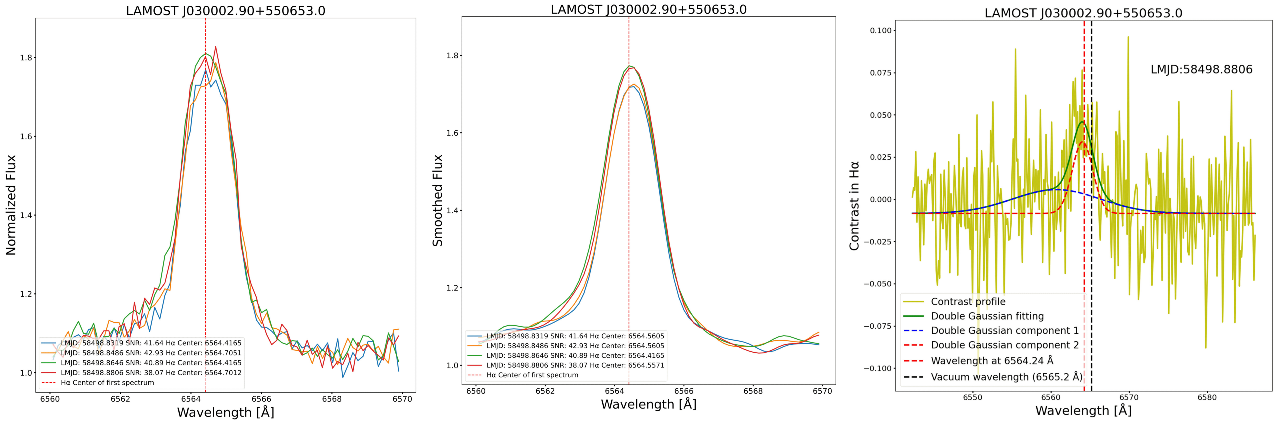

Fig. 21. Spectral analysis of the stellar $H\alpha$ lines and double-Gaussian fit. The left panel shows the preprocessed $H\alpha$ spectra of the star, the middle panel presents the smoothed $H\alpha$ spectra, and the right panel displays the contrast flux profile derived from the double-Gaussian fit.

to the Milky Way plane. In the one-dimensional z-axis image, we observed that the proportion of active stars decreases as the vertical distance from the Milky Way plane increases.

Using TESS data, we further investigated stellar flare events. By searching for flare events in the TESS light curves of 2868 stars, we identified 7496 flare events from 891 stars and calculated their flare energies, with an energy range from 2.15×10^{31} to 1.51×10^{36} erg. The results showed that the stellar chromospheric activity is positively correlated with stellar starspots, and the longer the flare duration, the higher the flare energy. By studying the $H\alpha$ line variations, we found an $EW_{H\alpha}$-like flare behavior in 119 M dwarfs and calculated the energy variation of $EW_{H\alpha}$ on short timescales, with an energy range from 6.12×10^{28} to 3.05×10^{35} erg. Twenty-five of these 119 M dwarfs showed flare events.

We searched for stellar CMEs based on the asymmetry features of the $H\alpha$ spectrum lines. Two of the 289 medium-resolution $H\alpha$ spectra with blue- or redshifted components showed a notable $H\alpha$ asmmetry. We classified them as CME candidates.

Data availability

Full Tables 1, 2, and 3 are only available at the CDS via `https://cdsarc.cds.unistra.fr/viz-bin/cat/J/A+A/704/A274`.

Acknowledgements. This research has been supported by the National Natural Science Foundation of China (NSFC) under Grant Nos. 12373032 and 11963002. Additionally, we acknowledge the use of data from the LAMOST survey, a National Major Scientific Project of the Chinese Academy of Sciences. The paper was also supported by Guizhou Provincial Major Scientific and Technological Program Nos. XKBF (2025) 010 and XKBF (2025)011.

References

Babcock, H. W. 1961, ApJ, 133, 572
Brito, A., & Lopes, I. 2019, MNRAS, 488, 1558
Bell, K. J., Hilton, E. J., Davenport, J. R. A., et al. 2012, PASP, 124, 911, 14
Canfield, R. C., Penn, M. J., Wulser, J.-P., et al. 1990, ApJ, 363, 318
Cao, D., Gu, S., Wolter, U., et al. 2023, MNRAS, 523, 4146
Chang, H.-Y., Song, Y.-H., Luo, A.-L., et al. 2017, ApJ, 834, 92
Cliver, E. W., Schrijver, C. J., Shibata, K., et al. 2022, LRSP, 19, 2
Chaplin, W. J., Bedding, T. R., Bonanno, A., et al. 2011, ApJ, 732, L5
Douglas, S. T., Agüeros, M. A., Covey, K. R., et al. 2014, ApJ, 795, 161
Du, B., Luo, A.-L., Zhang, S., et al. 2021, RAA, 21, 202
Davenport, J. R. A. 2016, ApJ, 829, 1, 23
Fang, X.-S., Zhao, G., Zhao, J.-K., et al. 2018, MNRAS, 476, 908
Feinstein, A. D., Montet, B. T., Ansdell, M., et al. 2020, AJ, 160, 219
Fetherolf, T., Pepper, J., Simpson, E., et al. 2023, ApJS, 268, 4
Frasca, A., Molenda-Żakowicz, J., De Cat, P., et al. 2016, A&A, 594, A39
Günther, M. N., Zhan, Z., Seager, S., et al. 2020, AJ, 159, 60
Gaia Collaboration (Vallenari, A., et al.) 2023, A&A, 674, A1
Gao, Q., Xin, Y., Liu, J.-F., et al. 2016, VizieR Online Data Catalog: J/ApJS/224/37
García Soto, A., Newton, E. R., Douglas, S. T., et al. 2023, AJ, 165, 192
García, R. A., Mathur, S., Salabert, D., et al. 2010, Science, 329, 1032
Gizis, J. E., Reid, I. N., & Hawley, S. L. 2002, AJ, 123, 3356
Green, M. J., Maoz, D., Mazeh, T., et al. 2023, VizieR Online Data Catalog: J/MNRAS/522/29
Han, H., Wang, S., Bai, Y., et al. 2023, ApJS, 264, 12
Hawley, S. L., Covey, K. R., Knapp, G. R., et al. 2002, AJ, 123, 3409
Hawley, S. L., Davenport, J. R. A., Kowalski, A. F., et al. 2014, ApJ, 797, 121
He, H., Wang, H., & Yun, D. 2015, ApJS, 221, 18
He, H., Wang, H., Zhang, M., et al. 2018, ApJS, 236, 7
He, L., Wang, S., Xu, X.-J., et al. 2019, RAA, 19, 098
Kossakowski, D., Espinoza, N., Brahm, R., et al. 2019, MNRAS, 490, 1094
Kruse, E. A., Berger, E., Knapp, G. R., et al. 2010, ApJ, 722, 1352
Koller, F., Leitzinger, M., Temmer, M., et al. 2021, A&A, 646, A34
Laughlin, G., Bodenheimer, P., & Adams, F. C. 1997, ApJ, 482, 420
Lee, K.-G., Berger, E., & Knapp, G. R. 2010, ApJ, 708, 1482
Li, J., Liu, C., Zhang, B., et al. 2021, ApJS, 253, 45
Lomb, N. R. 1976, Ap&SS, 39, 447
Long, L., Zhang, L.y., Bi, S.-L., et al. 2021, ApJS, 253, 51
Lu, H.p., Zhang, L.y., Shi, J., et al. 2019, ApJS, 243, 28
Lu, H.p., Tian, H., Zhang, L.y., et al. 2022, A&A, 663, A140
Luo, A.-L., Zhang, H.-T., Zhao, Y.-H., et al. 2012, RAA, 12, 1243
Luo, A.-L., Zhao, Y.-H., Zhao, G., et al. 2015, VizieR Online Data Catalog: V/146
Luo, A.-L., Zhao, Y.-H., Zhao, G., et al. 2022, VizieR Online Data Catalog: V/156
Maehara, H., Shibayama, T., Notsu, S., et al. 2012, Nature, 485, 478
Mamajek, E. E., & Hillenbrand, L. A. 2008, ApJ, 687, 1264
Maehara, H., Notsu, Y., Namekata, K., et al. 2021, PASJ, 73, 44
Muheki, P., Guenther, E. W., Mutabazi, T., et al. 2020, A&A, 637, A13
Mohanty, S., & Basri, G. 2003, ApJ, 583, 451
Mann, A. W., Dupuy, T., Kraus, A. L., et al. 2019, ApJ, 871, 63
Magaudda, E., Stelzer, B., Raetz, S., et al. 2022, A&A, 661, A29
McQuillan, A., Aigrain, S., & Mazeh, T. 2013, MNRAS, 432, 1203
Namekata, K., Sakaue, T., Watanabe, K., et al. 2017, ApJ, 851, 91
Newton, E. R., Irwin, J., Charbonneau, D., et al. 2017, ApJ, 834, 85
Noyes, R. W., Hartmann, L. W., Baliunas, S. L., et al. 1984, ApJ, 279, 763
Namekata, K., Maehara, H., Honda, S., et al. 2022, ApJ, 926, L5
Oliver, R., Soler, R., Terradas, J., et al. 2016, ApJ, 818, 128
Pineda, J. S., West, A. A., Bochanski, J. J., et al. 2013, AJ, 146, 50
Reiners, A., & Basri, G. 2008, ApJ, 684, 1390
Reiners, A., Joshi, N., & Goldman, B. 2012, AJ, 143, 93
Ricker, G. R., Winn, J. N., Vanderspek, R., et al. 2015, J. Astron. Teles. Instrum. Syst., 1, 014003
Scargle, J. D. 1982, ApJ, 263, 835
Sousa, S. G., Adibekyan, V., Santos, N. C., et al. 2019, MNRAS, 485, 3981
Shibata, K., & Magara, T. 2011, LRSP, 8, 6
Simon, T., & Drake, S. A. 1989, ApJ, 346, 303
Stelzer, B., Bogner, M., Magaudda, E., et al. 2022a, A&A, 665, A30
Stelzer, B., Caramazza, M., Raetz, S., et al. 2022b, A&A, 667, L9
Stassun, K. G., Oelkers, R. J., Paegert, M., et al. 2019, AJ, 158, 138
Salvato, M., Buchner, J., Budavári, T., et al. 2018, MNRAS, 473, 4937
Traven, G., Zwitter, T., Van Eck, S., et al. 2015, A&A, 581, A52
Trifonov, T., Kürster, M., Zechmeister, M., et al. 2018, A&A, 609, A117
Taylor, M. B. 2020, ADASS XXVII, 522, 67
Temmer, M. 2021, LRSP, 18, 4
Tu, Z.-L., Yang, M., Wang, H.-F., et al. 2021, ApJS, 253, 35
van Hoof, P. A. M. 2018, Galaxies, 6, 63
Walkowicz, L. M., Hawley, S. L., & West, A. A. 2004, PASP, 116, 1105
Wang, Y., Zhang, L., Su, T., et al. 2024, A&A, 686, A164
Walter, F. M. 1983, ApJ, 274, 794
Wenger, M., Ochsenbein, F., Egret, D., et al. 2000, A&AS, 143, 9
Wang, S., Bai, Y., He, L., et al. 2020, ApJ, 902, 2, 114
Watson, C. L., Henden, A. A., & Price, A. 2006, SASS, 25, 47
West, A. A., Hawley, S. L., Walkowicz, L. M., et al. 2004, AJ, 128, 426
West, A. A., Hawley, S. L., Bochanski, J. J., et al. 2008, AJ, 135, 785
West, A. A., Morgan, D. P., Bochanski, J. J., et al. 2011, AJ, 141, 97
Wright, N. J., Newton, E. R., Williams, P. K. G., et al. 2018, MNRAS, 479, 2351
Wu, Y., Chen, H., Tian, H., et al. 2022, ApJ, 928, 180
Xu, L., Zhang, L., Wang, Y., et al. 2025, A&A, 699, A322
Yang, H., Liu, J., Gao, Q., et al. 2017, ApJ, 849, 36
Yang, Z., Zhang, L., Meng, G., et al. 2023, A&A, 669, A15
Zhang, L., Pi, Q., Han, X. L., et al. 2016, New A, 44, 66
Zhang, L.-Y., Long, L., Shi, J., et al. 2020a, MNRAS, 495, 1252
Zhang, J., Bi, S., Li, Y., et al. 2020b, ApJS, 247, 1, 9
Zhang, L.y., Meng, G., Long, L., et al. 2021, ApJS, 253, 19
Zhang, L.y., Su, T., Misra, P., et al. 2023, ApJS, 264, 17

Appendix A: Examples of continuum placement and Hα_ EW measurement

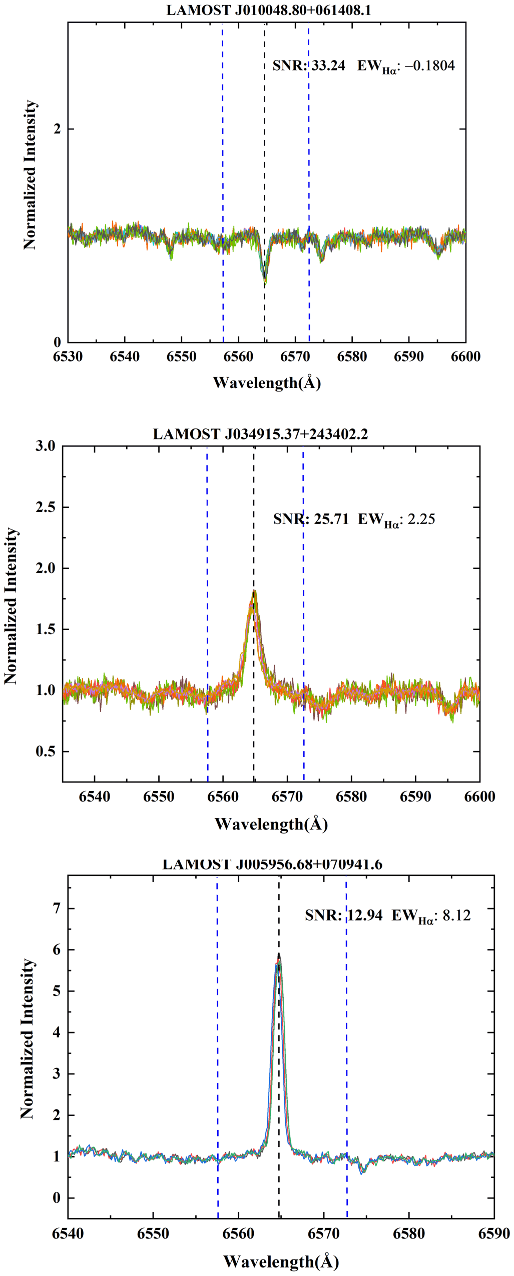

Fig. A.1. Examples of low-, moderate-, and high-activity stars showing the adopted ±25 Å continuum windows and fixed 15 Å integration region around the Hα line. The blue dashed vertical lines mark these spectral integration regions, illustrating the performance of our measurement method across different activity levels.